NASA Contractor Report 175036

Influence of Large-Scale Motion on Turbulent Transport for Confined Coaxial Jets

Volume II—Navier-Stokes Calculations of Swirling and Nonswirling Confined Coaxial Jets

Bernard C. Weinberg and Henry McDonald
Scientific Research Associates, Inc.
Glastonbury, Connecticut

January 1986

Prepared for
Lewis Research Center
Under Grant NAG 3-350

National Aeronautics and
Space Administration

SUMMARY

The multidimensional, ensemble-averaged, compressible, time-dependent Navier-Stokes equations are solved to predict the turbulent flow field resulting from confined swirling and nonswirling jets discharging into a suddenly expanded duct. The calculations which correspond to the experiments of Johnson and Bennett were conducted in a domain whose inflow boundary was situated upstream of the dump plane where the flow is unaffected by viscous interactions and extended downstream into the duct where the flow is fully developed. In order to be faithful to the actual experimental configuration, all sharp corners were retained and the inner jet wall was tapered. A two-equation k-ε turbulence model was employed to obtain the reported results. For the swirling case there was excellent qualitative and quantitative agreement with the experiments while for the nonswirling case qualitative agreement was obtained. The differences in agreement between the numerical predictions and the experimental data in the two cases appear to correspond to the effect of large scale coherent structures in the flow field. As determined in the companion paper by Brondum and Bennett, these large scale structures are dominant in the nonswirling case and may thus have a significant effect on the turbulence model, thereby leading to the discrepancies noted in the numerical computations. Furthermore, the calculations show that excessive artificial dissipation can have a dramatic effect on the overall flow structure, and must be effectively controlled to obtain accurate predictions.

INTRODUCTION

The design of modern gas turbine combusters is an extremely complex process. Many factors can influence their operation, including geometric effects, inflow properties of the air and fuel, turbulence of the flow and the overall mixing process. Obviously, methods that could aid in understanding and simulating these phenomena would be extremely useful in the design of more efficient combustors. Before considering the combustor as a whole includeing the combustion process, it is advantageous to consider the isothermal case. This allows study of individual nonreacting fluid dynamics phenomena, such as the effects of mass and momentum transport prior to considering the complications associated with reacting fluids. An understanding of these processes is a necessary prerequisite to the simulation of the more complex reacting flow field.

Recently Johnson and Bennett (Ref. 1) and Roback and Johnson (Ref. 2) have accumulated extensive experimental data for nonswirling and swirling turbulent flows in confined suddenly expanded coaxial jets. Since the experimental configurations were constructed to be similar to actual combustors and the Reynolds number under which the experiments were conducted was sufficiently high to assure fully turbulent flow, the data obtained from these experiments could be directly applied to the study of gas turbine combustors.

References 1 and 2 describe tne non-instrusive experiments conducted on a confined suddenly expanded coaxial jet. A schematic of the facililty is shown in Fig. 1. The working fluid was water which was circulated by a pump from the storage tank through the test section. Laser Velocimeter (LV) and Laser Induced Fluorescence (LIF) techniques were employed to obtain the data: velocities, concentrations and flow visualization. Details of the operation of the system are given in Refs. 1 and 2.

In association with these experiments numerical computations were performed (cf. Ref. 3) to model the flow fields. The results of these calculations indicated that several areas were in need of special attention; turbulence modeling, specification of upstream (inflow) boundary conditions and control of numerical or aritifical dissipation. With regard to turbulence modeling it should be noted that, a major objective of the experimental program was to obtain data bases from which a better

understanding and formulation of transport models could be obtained. In accordance with this goal the present effort was initiated to obtain accurate numerical computations which is a prerequisite in meeting the aims of the program. Concurrently Brondum and Bennett in the companion effort (Ref. 4) conducted experiments to isolate the effects of the large scale structures.

The effects of boundary conditions in general and inflow boundary conditions in particular play an important role in the flow development and, therefore, must be carefully chosen. In view of the strong interactions that occur between the coaxial jets, the subsequent strong mixing and the large recirculation zones that develop it is generally agreed that the full ensemble-averaged Navier-Stokes equations should be considered rather than simplified systems of equations. However, there is not universal agreement on how and where to specify boundary conditions. Implicit in the choice and application of "correct" boundary conditions is the choice of the appropriate computational domain. Recent results employing the TEACH code and its derivatives consider a rectangular domain with the upstream boundary being situated at the dump plane (cf. Ref. 3). In this computational domain one must specify at the dump plane not only the streamwise velocity and swirl velocity (if swirl is present), but also the normal velocity which is an extremely sensitive quantity. Furthermore, at the dump plane strong interactions between the jets occur so that it is not an optimum location at which to impose boundary conditions. Since the determiation of the flow properties at or near the dump plane is one of the objectives of the calculation, one cannot specify boundary conditions there.

In contrast to the procedure described above in the present calculations the upstream inflow boundary is placed upstream of the dump plane, where the flow properties are not influenced by the interaction process occurring at the dump plane. Further, the geometrical domain has been constructed to include a tapered inner wall for the central jet in order to model as best possible the actual experimental facility.

Navier-Stokes calculations were performed for the two cases considered in Refs. 1 and 2 employing a k-ε turbulence model. The Navier-Stokes solution procedure which was used in this effort was the consistently split

linearized block implicit (LBI) scheme of Briley and McDonald (Refs. 5 and and 6). The numerical scheme is embodied in a general computer code termed MINT (Multidimensional, Implicit, Nonlinear, Time-Dependent). The particular form of the code being used for the present application solves the general tensor form of the Navier-Stokes equations and, therefore, can be used with a general coordinate system. The dependent variables in the analysis are the velocity components, the density, and for turbulent flow if a two-equation model is used, the turbulence kinetic energy, k and the dissipation rate, ε. The results obtained compared well with the experiments in Refs. 1 and 2. In particular, for the nonswirling case there was excellent quantitative agreement with the data. Furthermore, the calculations indicate that numerical dissipation can have a significant effect on the numerical results.

ANALYSIS

The present analysis is based upon the solution of the ensemble-averaged Navier-Stokes equations using the linearized block implicit (LBI) method of Briley and McDonald (Ref. 5). The equations are solved in a constructive coordinate system with density and the velocity components being taken as dependent variables. The discussion of the coordinate system and governing equations is given next.

Coordinate System

In Fig. 2 is shown a schematic of the experimental facility with the pertinent dimensions (duplicated from Ref. 2). It consists of two coaxial pipes of inner and outer radii Ri_1 and Ra respectively expanding into a larger radius pipe of radius R_o with the inner pipe having a taper angle of 7.5 degrees. The computational domain chosen for the numerical computation was constructed to model this configuration as close as possible and is shown in Fig. 3.

There are several important features that are noteworthy. First, and foremost, the computational domain extends upstream of the dump phase, away from where the two jets mix. This allows for the specification of boundary conditions in a region unaffected by the mixing of the two jets which in general cannot be prescribed accurately. However, the computational domain introduces additional complications which must be taken into account by the solution procedure. These include reentrant corner points at the intersection of the inner pipe walls with the dump plane walls, and the introduction of surfaces where boundary layers develop and which must be resolved when no-slip boundary conditions are employed. In the case under consideration three reentrant corners are introduced. Note that although the inner central jet wall is tapered it terminates at the dump plane such that there is a finite thickness of the wall between the two jets. Furthermore, three additional walls have been introduced at Ri_1, Ri_2 and Ra, upstream of the dump plane where the respective boundary layers must be resolved. This places additional demands on the grid, viz. more grid points and/or grid clusterings are required.

The next feature of note is the inclusion of tapered inner wall at a nominal angle of 7.5° which corresponds to the actual experimental setup.

This tapered section is not a straight line, but rather consists of a cosine curve in order that the coordinate lines vary smoothly. By including this tapered portion, the grid becomes nonorthogonal, and must be taken into account in the analysis.

This geometry although more complicated than those considered by other researchers (e.g. Ref. 3) is more realistic and is, therefore, employed. Nevertheless, the nonorthogonal geometry and the reentrant corners requires no additional code modifications since the MINT procedure has been designed to treat such cases.

The upstream boundary was placed at 51.0 mm upstream of the dump plane to correspond to the location where the swirler was placed and was employed for the nonswirl case as well. The downstream boundary was placed at 14.0 R_o downstream, where fully turbulent conditions should be recovered.

The grid consisted of 91 grid points in the radial direction and 71 points in the streamwise direction. The grid was clustered as noted above to resolve the boundary layers on all solid surfaces. The solid surfaces correspond as the following radial grid point locations

$$R_{i1} = 28$$
$$R_{i2} = 31$$
$$Ra = 63$$
$$R_o = 91$$

In the streamwise direction, there were 71 grid points with the dump plane located at grid point 15. The maximum grid spacing was at the downstream boundary, $\Delta Z_{max} = .70\ R_o$, and the minimum spacing at the dump plane was $\Delta Z_{min} = .01\ R_o$. The family of radial lines were straight while the streamwise curves conformed to the body shape. As noted above, this led to a nonorthogonal coordinate system, and is shown in Fig. 4. Note that downstream of the dump plane the streamwise coordiante curves are adjusted to cluster more points near the centerline. To achieve the grid clustering, a transformation due to Oh (Ref. 8) was employed.

Governing Equations

The equations used in the present effort are the ensemble-averaged, time-dependent Navier-Stokes equations which can be written in vector form as

Continuity

$$\frac{\partial \rho}{\partial t} + \nabla \cdot \rho \vec{U} = 0 \tag{1}$$

Momentum

$$\frac{\partial \rho \vec{U}}{\partial t} + \nabla \cdot (\rho \vec{U}\vec{U}) = -\nabla P + \nabla \cdot (\bar{\bar{\pi}} + \pi^T) \tag{2}$$

Energy

$$\frac{\partial \rho h}{\partial t} + \nabla \cdot (\rho \vec{U} h) = -\nabla \cdot (\vec{Q} + \vec{Q}^T) + \frac{DP}{Dt} + \Phi + \rho\epsilon \tag{3}$$

where ρ is density, U is velocity, p is pressure, π is the molecular stress tensor π^T is the turbulent stress tensor, h is enthalpy, Q is the mean heat flux vector, Q^T is the turbulent heat flux vector, Φ is the mean flow dissipation rate and ϵ is the turbulence energy dissipation rate. If the flow is assumed as a constant total temperature, the energy equation is replaced by

$$T_t = T + \frac{q^2}{2C_p} = \text{constant} \tag{4}$$

where T_t is the stagnation temperature, q is the magnitude of the velocity and C_p is the specific heat at constant pressure. In the cases considered in this work, constant total temperature has been assumed. A number of terms appearing in Eqs. 1 - 3 require definition. The stress tensor appearing in Eq. 2 is defined as

$$\bar{\bar{\pi}} = 2\mu \mathbb{D} - \left(\frac{2}{3}\mu - K_B\right) \nabla \cdot \vec{U} \mathbb{I} \tag{5}$$

where K_B is the bulk viscosity coefficient, I is the identity tensor, and $\mathbb{D}$ is the deformation tensor, defined by:

$$\mathbb{D} = \frac{1}{2}\left((\nabla \vec{U}) + (\nabla \vec{U})^T\right) \tag{6}$$

In addition, the turbulent stress tensor has been modeled using an isotropic eddy viscosity such that:

$$\pi^T = -\rho \overline{\vec{u}'\vec{u}'} = 2\mu_T \mathbb{D} - \frac{2}{3}(\mu_T \nabla \cdot \vec{U} + \rho K) I \tag{7}$$

where, k is the turbulent kinetic energy and μ_T, the turbulent viscosity, is determined by a suitable turbulence model. Turbulence modelling is described in some detail in the next section.

Equation 8 contains a mean heat flux vector defined as follows:

$$\vec{Q} = -\kappa \nabla T \tag{8}$$

and a turbulent heat flux vector defined as:

$$\vec{Q}^T = -\kappa^T \nabla T \tag{9}$$

where κ and κ^T are the mean and turbulent thermal conductivities, respectively.

Also appearing in Eq. 3 is the mean flow dissipation term Φ.

$$\Phi = 2\mu \mathbb{D} : \mathbb{D} - (\frac{2}{3}\mu - K_B)(\nabla \cdot \vec{U})^2 \tag{10}$$

The equation of state for a perfect gas

$$P = \rho R T \tag{11}$$

where R is the gas constant, the caloric equation of state

$$e = C_v T \tag{12}$$

and the definition of static enthalpy

$$h = C_p T \tag{13}$$

supplement the equations of motion.

Finally the flow properties μ, κ and K_B are determined using the following constitutive relations.

The molecular viscosity μ is determined using Sutherland's law.

$$\frac{\mu}{\mu_0} = \left(\frac{T}{T_0}\right)^{3/2} \frac{T_0 + S_1}{T + S_1} \tag{14}$$

where S_1 = 100°K for air.

The bulk viscosity is assumed to be zero

$$K_B = 0 \tag{15}$$

and the thermal conductivity is determined by use of a relation similar to Sutherland's law viz.

$$\frac{\kappa}{\kappa_0} = \left(\frac{T}{T_0}\right)^{3/2} \frac{T_0 + S_2}{T + S_2} \tag{16}$$

where $S_2 = 194°k$ for air.

Dependent Variables and Coordinate Transformation

The set of governing partial differential equations which model the physical processes was presented in the previous section. For generality these equations were written in vector notation; however, before these equations can be incorporated into a computer code, a coordinate system must be chosen. The governing equations can then be cast in a form reflecting the choice of the coordinate system. Therefore, the governing equations written in a cylindrical polar coordinate system are transformed with a general Jacobian transformation of the form

$$\begin{aligned} y^j &= y^j(\bar{x}_1, \bar{x}_2, \bar{x}_3, t) \\ \tau &= t \end{aligned} \tag{17}$$

where $(\bar{x}_1, \bar{x}_2, \bar{x}_3)$ are the original coordinates (Ref. 9). In cylindrical polar coordinates $\vec{(x_1)}$ would correspond to (r, θ, z). The velocity components remain the components, (U_1, U_2, U_3) in the $(\bar{x}_1, \bar{x}_2, \bar{x}_3)$ coordinate directions, respectively. The new independent variables y^j are the computational coordinates in the transformed system. The coordinate system requirements for the problem under consideration may be represented by a subset of the general transformation, Eq. (17)

$$\begin{aligned} y^1 &= y^1(x_1, x_3, t) \\ y^2 &= y^2(x_2) \\ y^3 &= y^3(x_1, x_3, t) \end{aligned} \tag{18}$$

which is a general axisymmetric time-dependent transformation. For the coaxial jet configuration which is axisymmetric, Eq. (18) reduces to $y^2 = \bar{x}_2$ and all derivatives $\partial/\partial y^2$ are assumed to be zero.

Application of the Jacobian transformation requires expansion of the temporal and spatial derivatives using the chain rule, i.e.,

$$\frac{\partial \phi}{\partial t} = \frac{\partial \phi}{\partial \tau} + \sum_{j=1}^{3} y^j_{,t} \frac{\partial \phi}{\partial y^j} \tag{19}$$

and

$$\frac{\partial \phi}{\partial \bar{x}_i} = \sum_{j=1}^{3} y^j_{,i} \frac{\partial \phi}{\partial y^j} \tag{20}$$

where

$$y^j_{,t} \equiv \frac{\partial y^j}{\partial t}$$

$$y^j_{,i} \equiv \frac{\partial y^j}{\partial \bar{x}_i} \tag{21}$$

The relations Eqs. (19-21) are first substituted into the governing equations (1-4) written in Cartesian or cylindrical polar coordinates. Then the resulting equations are multiplied by the Jacobian determinant of the inverse transformation,

$$J = \frac{\partial(\bar{x}_1, \bar{x}_2, \bar{x}_3)}{\partial(y^1, y^2, y^3)} = \begin{vmatrix} \frac{\partial \bar{x}_1}{\partial y^1} & \frac{\partial \bar{x}_1}{\partial y^2} & \frac{\partial \bar{x}_1}{\partial y^3} \\ \frac{\partial \bar{x}_2}{\partial y^1} & \frac{\partial \bar{x}_2}{\partial y^2} & \frac{\partial \bar{x}_2}{\partial y^3} \\ \frac{\partial \bar{x}_3}{\partial y^1} & \frac{\partial \bar{x}_3}{\partial y^2} & \frac{\partial \bar{x}_3}{\partial y^3} \end{vmatrix} \tag{22}$$

and the equations are cast into a "semi-strong" conservation form (Ref. 9) using the following relations,

$$\sum_{j=1}^{3} \frac{\partial (J y^j_{,i})}{\partial y^j} = 0 \tag{23}$$

and

$$\frac{\partial J}{\partial \tau} + \sum_{j=1}^{3} \frac{\partial J y^{j}_{,t}}{\partial y^{j}} = 0 \tag{24}$$

The semi-strong conservation form implies that all factors involving the radial coordinate $r = \bar{x}_1$ remain as they were before the Jacobian transformation. The resulting equations are presented in Appendix B.

The geometric relations Eq. (23-24) may be obtained from the transformation relations for $J\dot{y}^{j}_{,t}$ and $J\dot{y}^{j}_{,i}$ in terms of the inverse transformation derivatives (e.g., Ref. 10),

$$\begin{aligned}
J\dot{y}^{1}_{,1} &= \bar{x}_{2,2}\,\bar{x}_{3,3} - \bar{x}_{2,3}\,\bar{x}_{3,2} \\
J\dot{y}^{1}_{,2} &= \bar{x}_{3,2}\,\bar{x}_{1,3} - \bar{x}_{3,3}\,\bar{x}_{1,2} \\
J\dot{y}^{1}_{,3} &= \bar{x}_{1,2}\,\bar{x}_{2,3} - \bar{x}_{1,3}\,\bar{x}_{2,2} \\
J\dot{y}^{2}_{,1} &= \bar{x}_{2,3}\,\bar{x}_{3,1} - \bar{x}_{2,1}\,\bar{x}_{3,3} \\
J\dot{y}^{2}_{,2} &= \bar{x}_{3,3}\,\bar{x}_{1,1} - \bar{x}_{3,1}\,\bar{x}_{1,3} \\
Jy^{2}_{,3} &= \bar{x}_{1,3}\,\bar{x}_{2,1} - \bar{x}_{1,1}\,\bar{x}_{2,3} \\
J\dot{y}^{3}_{,1} &= \bar{x}_{2,1}\,\bar{x}_{3,2} - \bar{x}_{2,2}\,\bar{x}_{3,1} \\
J\dot{y}^{3}_{,2} &= \bar{x}_{3,1}\,\bar{x}_{1,2} - \bar{x}_{3,2}\,\bar{x}_{1,1} \\
J\dot{y}^{3}_{,3} &= \bar{x}_{1,1}\,\bar{x}_{2,2} - \bar{x}_{1,2}\,\bar{x}_{2,1}
\end{aligned} \tag{25}$$

and

$$J\dot{y}^{j}_{,t} = -\sum_{k=1}^{3} J\dot{y}^{j}_{,k}\,\frac{\partial \bar{x}_k}{\partial \tau} \tag{26}$$

Turbulence Modeling

Several alternative turbulence models can be applied to the problem at hand. In general terms, these models are the zero-, and two-equation models. The formulation of each of the two is described in this section.

Zero Equation Model - (Mixing Length)

Of all available turbulence models, Prandtl's mixing length model is probably still the most widely used. The model was originally developed for use in unseparated boundary layer flow situations and has been shown to perform well under such conditions. An advantage of the method from the point of view of economy is that it does not require additional transport equations to model the effect of turbulence, but rather relates the Reynolds' shear stress to mean flow quantities via:

$$-\overline{\rho u_i' u_j'} = \mu_T \frac{\partial U_j}{\partial x_i}$$

where

$$\mu_T = \rho \ell^2 (2\mathbb{D} : \mathbb{D})^{1/2}$$

and

$$\ell = \min\left[\ell_\infty, \kappa d D \right]$$

where d is the normal distance to the nearest wall and D is the van Driest damping coefficient given by

$$D = 1 - \exp(-y^+ / A^+) \qquad y^+ = d u_\tau / \upsilon$$

$$\ell_\infty = 0.09\delta \qquad u_\tau = (\tau_\ell / \rho)^{1/2} \qquad (27)$$

$$\kappa = 0.4$$

and where the local shear stress τ_ℓ is obtained from

$$\tau_\ell = (2\mathbb{D} : \mathbb{D})^{1/2} \qquad (28)$$

and $\mathbb{D}$ is defined by Eq. 6.

One problem in the mixing length formulation is the definition of δ, which for flows of the type considered here is extremely difficult to estimate. Hence, it has not been used to obtain the reported flow fields. However, as will be discussed in the following sections, this model is used to initialize the computations.

Two-Equation Model - (k-ε)

As discussed above, the mixing length concept is valid for a variety of flows, in which the viscous layer is wall bounded. However, in cases such as considered here which involve large reciruclation zones, and is shear dominated, a less restrictive model is required. One such model is the two-equation turbulence model (Refs. 11-15) in which a transport equation for turbulence kinetic energy, k, is formulated as follows:

$$\frac{\partial \rho K}{\partial t} + \nabla\cdot(\rho \vec{U} K) = \nabla\cdot\left(\frac{\mu_T}{\sigma_K}\nabla K\right) + 2\mu_T(\mathbb{D}:\mathbb{D}) - \rho\epsilon - 2\rho\nu(\nabla K^{1/2})^2 \tag{29}$$

where k is the turbulence kinetic energy and is defined as

$$K = \frac{1}{2}\overline{\vec{u}'\cdot\vec{u}'} \tag{30}$$

and the transport equation for the dissipation ε is

$$\frac{\partial \rho \epsilon}{\partial t} + \nabla\cdot(\rho \vec{U} \epsilon) = \nabla\cdot\left(\frac{\mu_T}{\sigma_\epsilon}\nabla\epsilon\right) + C_1(2\mu_T\mathbb{D}:\mathbb{D})\frac{\epsilon}{K} + 2\mu\mu_T(\nabla^2 U)^2 - C_2\rho\frac{\epsilon^2}{K} \tag{31}$$

However, attempts to solve Eqs. 29 and 31 without modification present problems because an appropriate boundary condition for ε at a solid boundary is difficult to prescribe such that Eq. 31 is satisfied. Following the suggestion of Jones and Launder (Ref. 12), the turbulence dissipation equation has been modified by the inclusion of the term:

$$-2\mu\mu_T(\nabla^2 U)^2$$

in the energy dissipation equation, Eq. (31), and by the inclusion of the term:

$$-2\rho\nu(\nabla K^{1/2})^2$$

in the turbulence energy equation. These additional terms allow an $\epsilon = o$ wall boundary condition to be applied and appear to correctly model the near wall region as discussed in Ref. 12. Following Ref. 12, the following empirical relations are used.

$$\sigma_\epsilon = 1.3 \qquad \sigma_k = 1.0$$

$$C_1 = 1.43$$

$$C_\mu = 0.09 \exp\left[-2.5/(1 + R_\tau/50)\right]$$

$$C_2 = 1.92\left[1.0 - 0.3 \exp(-R_\tau^2)\right]$$

and R_τ is defined as:

$$R_\tau = \frac{\rho k^2}{\mu\epsilon}$$

The Prandtl-Kolmogorov relation, defines the turbulent viscosity as:

$$\mu_T = C_\mu \frac{\rho K^2}{\epsilon} \tag{32}$$

In modeling the flow in the near wall region where low local turbulence Reynolds' numbers occur, two approaches are available. The first is the wall function approach which does not resolve the near wall region but assumes specific function forms for the required turbulence quantities and uses these forms to create the required normal derivative formulations at the first grid point from the wall. Such an approach obviously requires a detailed knowledge of the turbulence model dependent variables in the vicinity of the wall. Although reasonable function formulations can be specified for simple two-dimensional flows such as constant pressure boundary layers, specification in the much more complex flows of current interest is much more difficult. Therefore, the alternative approach in which the viscous sublayer is resolved has been used. The method makes no approximation at the boundary, but requires that the near wall low turbulence Reynolds' number physics be modeled.

Initial and Boundary Conditions

Steady solution of the system of governing partial differential equations represented by Equations (1-3) is obtained by time marching these equations until a steady state is reached. Before the solution procedure is described two important aspects must be discussed: (1) the initial conditions and (2) the boundary conditions. Any procedure which utilizes either a time marching method to obtain a steady state (or transient) solution or a Newton-Raphson iteration procedure requires some initial guess of the flow variables (in this case all the dependent variables and other necessary variables such as pressure, temperature, viscosity, etc.). In some of the simpler cases, some reasonable approximation to a converged solution can either be guessed or obtained through physical reasoning. However, since the flow field considered under this effort is dominated by large recirculation zones it was felt that an initial guess containing such closed vortical patterns would be very difficult at best and at worst could hamper the ultimate convergence history. The approach taken here was to assume that the flow was initially stagnant (all velocity components were set to zero), and that the pressure and temperature were constant being set equal to the downstream exit flow conditions. The upstream velocity profiles were then raised to some precribed level over a period of time thereby driving the flow through the duct. Thereafter the solution was marched out in time until a steady state was achieved. This technique has the advantage of being easy to implement in any geometric configuration.

To obtain a solution of the governing system of partial differential equations represented by Equations (1-3), it is necessary to define boundary conditions on each bounding surface of the computational domain. For the purposes of this investigation boundary conditions can be classified as occurring on two different types of bounding surfaces: (1) walls on solid surfaces, (2) inlets and exits. The boundary condition utilized on each different type of surface will now be discussed in turn.

At walls and solid boundaries no slip is prescribed, i.e. the streamwise and normal velocities are set to zero. In addition the normal pressure gradient is set to zero. As an alternate boundary condition the normal momentum equation can be solved at the boundary, and is employed if required by the physics of the flow.

At the outflow boundary, for subsonic flow the static pressure is specified and the velocity components are extrapolated, i.e. the second derivatives of the streamwise and normal velocities are set to zero. The inflow boundary, however requires some additional care. Since the velocity profiles at the inlet were measured (cf. Ref. 7), they were specified there and were fixed throughout the calculation. This essentially sets the mass flow through the system. An additional boundary condition is needed for density, which for this case reduced to an extrapolation condition.

As a final note, a description is given of the treatment of the reentrant corners, which appear as geometrical singularities in the flow. The specification of no slip offers no difficulty at these corners, since the velocities are set identically to zero. However, the pressure condition is somewhat more difficult since it involves a derivative. In order to circumvent the difficulty associated with choosing the direction in which the normal derivative is to be taken, the corner is treated as a double valued point. Hence, two values of pressure (and density) are stored, each corresponding to the direction in which the coordinate lines approach the corner. Although this method is approximate, it has worked well in practice and does not appear to adversely affect the results obtained.

Numerical Procedure

The numerical procedure used to solve the governing equations is the consistently split linearized block implicit (LBI) scheme originally developed by Briley and McDonald (Ref. 5). A conceptually similar scheme has been developed for two-dimensional MHD problems by Lindemuth and Killeen (Ref. 16). The procedure is discussed in detail in Refs. 5 and 6. The method can be briefly outlined as follows: the governing equations are replaced by an implicit time difference approximation, optionally a backward difference or Crank-Nicolson scheme. Terms involving nonlinearities at the implicit time level are linearized by Taylor expansion in time about the solution at the known time level, and spatial difference approximations are introduced. The result is a system of multidimensional coupled (but linear) difference equations for the dependent variables at the unknown or implicit time level. To solve these difference equations, the Douglas-Gunn (Ref. 17) procedure for generating alternating-direction implicit (ADI) schemes as perturbations of fundamental implicit difference schemes is introduced in its

natural extension to systems of partial differential equations. This technique leads to systems of coupled linear difference equations having narrow block-banded matrix structures which can be solved efficiently by standard block-elimination methods.

The method centers around the use of a formal linearization technique adapted for the integration of initial-value problems. The linearization technique, which requires an implicit solution procedure, permits the solution of coupled nonlinear equations in one space dimension (to the requisite degree of accuracy) by a one-step noniterative scheme. Since no iteration is required to compute the solution for a single time step, and since only moderate effort is required for solution of the implicit difference equations, the method is computationally efficient; this efficiency is retained for multidimensional problems by using what might be termed block ADI techniques. The method is also economical in terms of computer storage, in its present form requiring only two time-levels of storage for each dependent variable. Furthermore, the block ADI technique reduces multi-dimensional problems to sequences of calculations which are one-dimensional in the sense that easily-solved narrow block-banded matrices associated with one-dimensional rows of grid points are produced. A more detailed discussion of the solution procedure as discussed by Briley, Buggeln and McDonald (Ref. 18) is given in the Appendix A.

Artificial Dissipation

Since the calculations of interest are often at high Reynolds numbers typical of combuster flow fields, it is necessary to suppress spatial oscillations associated with central spatial differences approximations. This can be done via a dissipative spatial difference formulation (e.g., one-sided difference approximations for first derivatives) or by explicitly adding an additional dissipative type term. For the Navier-Stokes equations, the present authors favor the latter approach since when an additional term is explicitly added, the physical approximation being made is clearer than when dissipative mechanisms are contained within numerical truncation errors, and further, explicit addition of an artificial dissipation term allows greater control over the amount of non-physical dissipation being added. Obviously, the most desirable technique would add

only enough dissipative mechanism to suppress oscillations without deteriorating solution accuracy. Various methods of adding artificial dissipation were investigated in Ref. 20, and these were evaluated in the context of a model one-dimensional problem containing a shock with a known analytic solution (one-dimensional flow with heat transfer). The methods which were considered included second-order dissipation, fourth-order dissipation and pressure dissipation techniques.

As a result of this investigation, it was concluded that a second-order anisotropic artificial dissipation formulation suppressed spatial oscillations without impacting adversely on acccuracy. In the present application a term of the form

$$\frac{\partial}{\partial x_j}\left[(\mu_{art})_j \frac{\partial \phi}{\partial x_j}\right]$$

is added to the governing equations for each coordinate direction j. The variable ϕ denotes the velocity component U_i for the x_i-direction momentum equation, the density ρ for the continuity equation, and the enthalpy h for the energy equation. The coefficient $(\mu_{art})j$ is obtained from

$$\rho U_j \Delta x_j \leq (1/\sigma_d)(\bar{\mu} + (\mu_{art})_j)$$

where Δxj is the grid spacing at the point in question. The quantity $\bar{\mu}$ denotes the effective viscosity (μ_{eff}) for the momentum equations, (μ_{eff}/Pr) for the energy equation, (μ_{eff}/σ_k) for the turbulence kinetic energy equation, ($\mu_{eff}/\sigma_\epsilon$) for the turbulence dissipation equation, and is zero for the continuity equation.

The question arises as to the values of σ_x and σ_y which should be chosen. This was assessed both through model problems (Ref. 19), and through actual calculations (Refs. 19, 20 and 21). These results indicated that values of $\sigma = .5$ which corresponds to a cell Reynolds number 2 limitation would severely damp physical variations. However, when σ was set in the range $.05 < \sigma < 0.10$, which correspond to a cell Reynolds number range

between 20 and 10, spurious spatial oscillations were damped with no significant change in the calculated results as σ was varied in this range. Further, as discussed in Refs. 19-21, the results obtained showed good agreement with data.

DISCUSSION OF RESULTS

As discussed in previous sections, the computation of the flow field was initiated from quiescent conditions. During the initial transient phase the upstream velocity profile was augmented until its magnitude matched the experimental values of Johnson (Ref. 7). Once the profiles were attained, they were fixed for the duration of the calculation.

The velocity profiles that were employed were obtained from curve fits of Johnson's experimental data (Ref. 7) which was taken at 41mm upstream of the dump plane using a hot film probe. For the inner pipe a log law profile in conjunction with a viscous sublayer was fit to the data. With the constants in the log law formula fixed, the sole parameter is the friction velocity u_τ, which was determined by a Newton iteration procedure.

In the annulus, the formulas presented by Bird, Stewart and Lightfoot (Ref. 22, Eqs. 5.F-2 and 5.F-3) were used to fit the streamwise velocity data.

$$u_{max} - u = \frac{1}{\kappa_1} u_\tau \left[\frac{k^2 - \lambda^2}{k}\right]^{1/2} \ln\left[\frac{(\lambda - k)R}{r - kR}\right] \qquad r < \lambda R$$

$$u_{max} - u = \frac{1}{\kappa_1} u_\tau \sqrt{1 - \lambda^2} \ln\left[\frac{R - \lambda R}{R - r}\right] \qquad r > \lambda R$$

where $k_1 = .4$, $k = R_i/R_o$ and $r = \lambda R_o$ is the point of maximum velocity. Since each formula is singular at the inner and outer walls, these formulas were supplemented by additional equations that account for the viscous sublayer. Here again the only free parameters were the two friction velocities at the respective walls, and were determined by using a Newton iteration procedure.

The k and ε distributions at the upstream boundaries were also obtained from the experimental data given in Ref. 6. In contrast to the curve fit procedure used for the streamwise velocity distribution, for k and ε local piecewise parabolic polynomials were employed. The curve fits also prescribed zero values for k and ε at the walls consistent with the boundary conditions used in the calculation procedure.

For the swirling case, the swirl velocity distribution was also required at the upstream boundary. Since that data was not given, an alternate

procedure was employed to obtain the swirl velocity profiles. A comparison of the nonswirling axial velocity profiles at the upstream station and at 5mm downstream of the dump plane showed that the core velocity profile away from the walls does not vary significantly for the two cases. Hence, it was assumed that similar behavior should hold for the swirl or azimuthal velocity profile. Therefore, the data given at z = 5mm downstream of the dump plane was used to obtain the required velocity profiles. The curve fit procedure employed was identical to the nonswirling case in which the data was fit with logarithmic profiles in conjunction with a laminar sublayer.

Both the swirling and nonswirling cases were computed for a Reynolds number of 35,000 based on duct diameter. The nonswirling case was run first employing an artificial dissipation parameter of $\sigma = .5$. The results were very similar to coarse grid calculations considered previously. Initially, the nonswirl case was computed on a coarser grid of 61 x 51 grid points. This calculation differed from that which is described in this report in two respects. First, the inner jet wall was untapered and second, the upstream velocity profiles were "guessed" since at that time no experimental data was available. The results were substantially the same as the current nonswirling case which is described subsequently. Hence, grid resolution was not the prime source of the discrepancies.

The streamwise velocity profiles across the duct at various downstream stations are shown in Fig. 5. As can be seen, there is fairly good agreement between the data and the predictions. However, the axial velocity variation along the centerline which is shown in Fig. 6 does not compare as well. In Fig. 6 the present calculations are plotted against the experimental data, and the predictions of Ref. 3 which uses a different numerical procedure, but a similar $k-\varepsilon$ turbulence model. Both computations indicate a dip in the axial velocity which is not observed in the experiments. The precise reasons for this behavior is uncertain, but turbulence modeling appears to be the most likely culprit. In view of the good agreement with data that was obtained for the swirling case, the source of the discrepancies must lie in the distinguishing characteristics of the two flows. In reference 4, Brondum and Bennet determined the presence of large scale coherent structures in the nonswirling case. Furthermore their major effect was precisely in those regions which showed the greatest deviation from the experimental data.

Therefore, it would appear that the κ-ε tranport equations should be investigated to determine how they can be modified to account for the phenomena observed in the experiments.

In Fig. 7 the streamline pattern and in Fig. 8 contours of constant axial velocity profiles are shown. The recirculation zone which develops along the duct wall extends approximately four duct radii downstream of the dump plane, and compares well with the experimental data.

Since the emphasis of the present effort was to demonstrate the capabilities of the numerical scheme, the resolution of the descrepancies were not pursued further, but rather the swirling case was considered. As initial conditions, the nonswirl flow field was employed and thereafter the swirl velocity was introduced at the inflow boundary in the annulus over a prescribed number of time steps. Two cases were considered at two different values of artificial dissipation parameter σ. The values of the parameter σ were .5 and .1, a lower value indicating less dissipation.

The results of the computations are shown in Figs. 9 to 14. Both σ = .5 and .1 computations are shown. In Fig. 9 the streamline patterns are shown. As can be seen, there is a significant variation in the flow patterns in particular in the shape and extent of the recirculation zones. Similar differences in the two calcultions can be seen in Figs. 10 and 11 where the contours of constant streamwise and azimuthal (swirl) velocities are shown.

A more dramatic effect is seen in Figs. 12 to 13 where the axial and azimuthal velocity profiles are shown at different streamwise locations in the duct. The σ = .1 calculations are in excellent agreement with the data. Compared with the σ = .5 solution, the effect of artificial dissipation is clearly evident, in the smearing of the profiles and the cutting off of the peaks. The final plot figure 14 shows the streamwise velocity distribution along the duct. Here again the effect of reduced artificial dissipation is evident, in that the computed results are in better agreement with the experimental data.

In comparing the streamwise velocity distributions along the duct, it is noted that the velocity at the dump plane is lower than the experimental value. Hence, there appears to be a discrepancy with regard to the mass flow through the system. Inasmuch as the parameter describing the flow is the Reynolds number, the discrepancy in mass flow would vary the Reynolds number under which the calculation was run. The reasons for the discrepancies in

mass flux are uncertain, but errors in the specificaton of inflow profiles could have played a role. Furthermore, the choice to set function conditions at the upstream inflow boundary may have also contributed to the observed discrepancies. For subsonic inflow, the preferred inflow boundary condition is to set the stagnation pressure, and let the streamwise velocity profile adjust to accomodate the mass flux. Since the stagnation pressure was unavailable, the mass flux was specified instead. It is felt that further investigation is warranted with regard to this aspect of the calcuation.

CONCLUSIONS

Navier-Stokes calculations employing a k-ε turbulence model were obtained for the flow resulting from confined swirling and nonswirling confined coaxial jets. The calculations compared well with the experimental data of Johnson and Bennet and Roback and Johnson, in particular for the swirling case. The calculations indicate that, as long as the turbulence model is well specified, the numerical procedure can give results that compare very well with the data. Furthermore the results demonstrate that artificial or numerical dissipation can have a significant effect on the computations and must be carefully controlled to obtain accurate predictions.

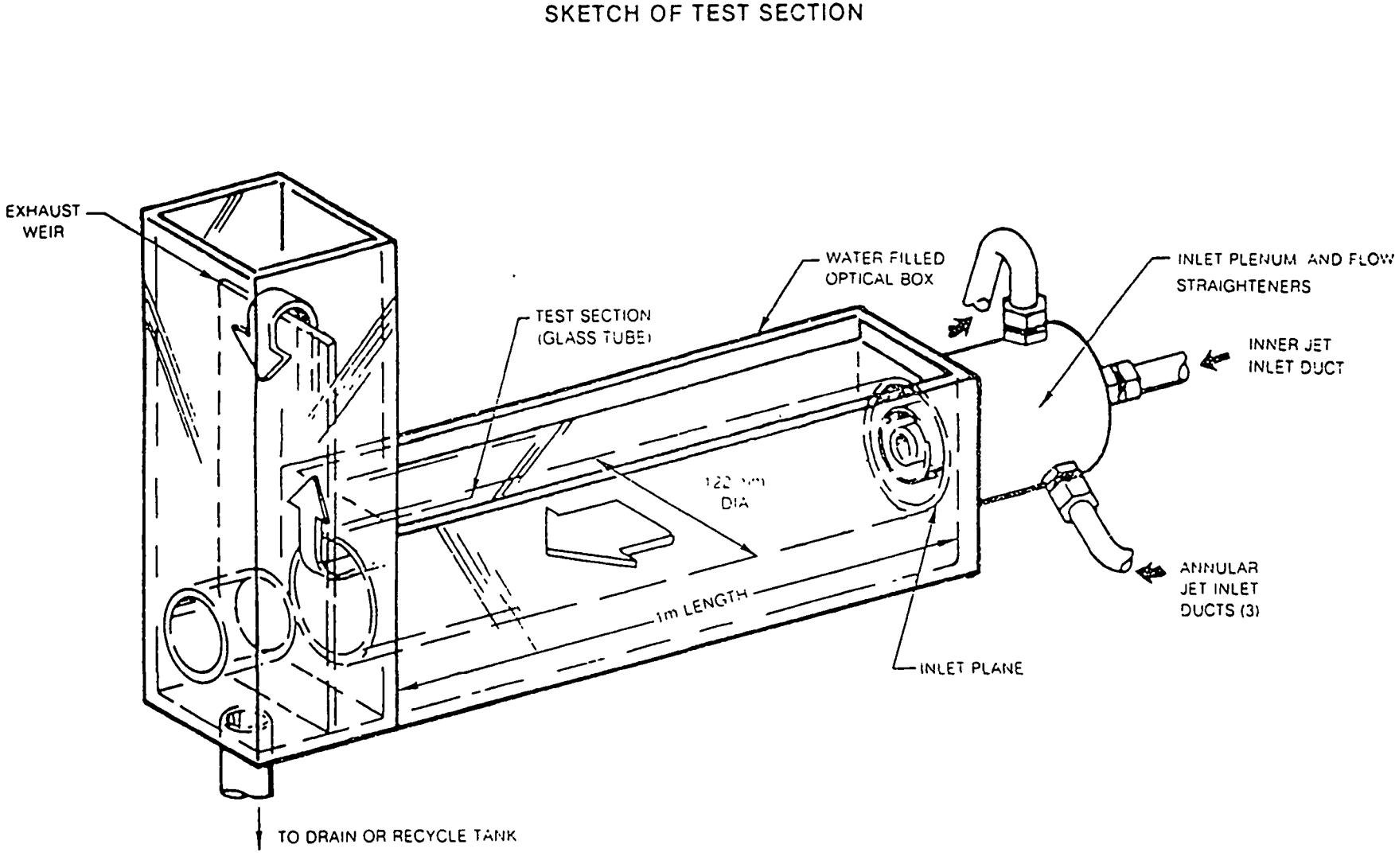

Figure 1. Sketch of Experimental Test Section (from Ref. 2).

SKETCHES OF TEST SECTION INLET REGION WITH VELOCITY AND COORDINATE SYSTEM

30 DEG MEAN ANGLE SWIRLER IN ANNULAR INLET DUCT

DIMENSION	R_{i1}	R_{i2}	R_a	R_o	S	L
LENGTH (mm)	12 5	15 3	29 5	61 0	51	1016
LENGTH (in)	0 492	0 601	1 162	2 402	2 0	40
RADIUS RATIO, r/R_o	0 205	0 251	0 484	1 0	–	–

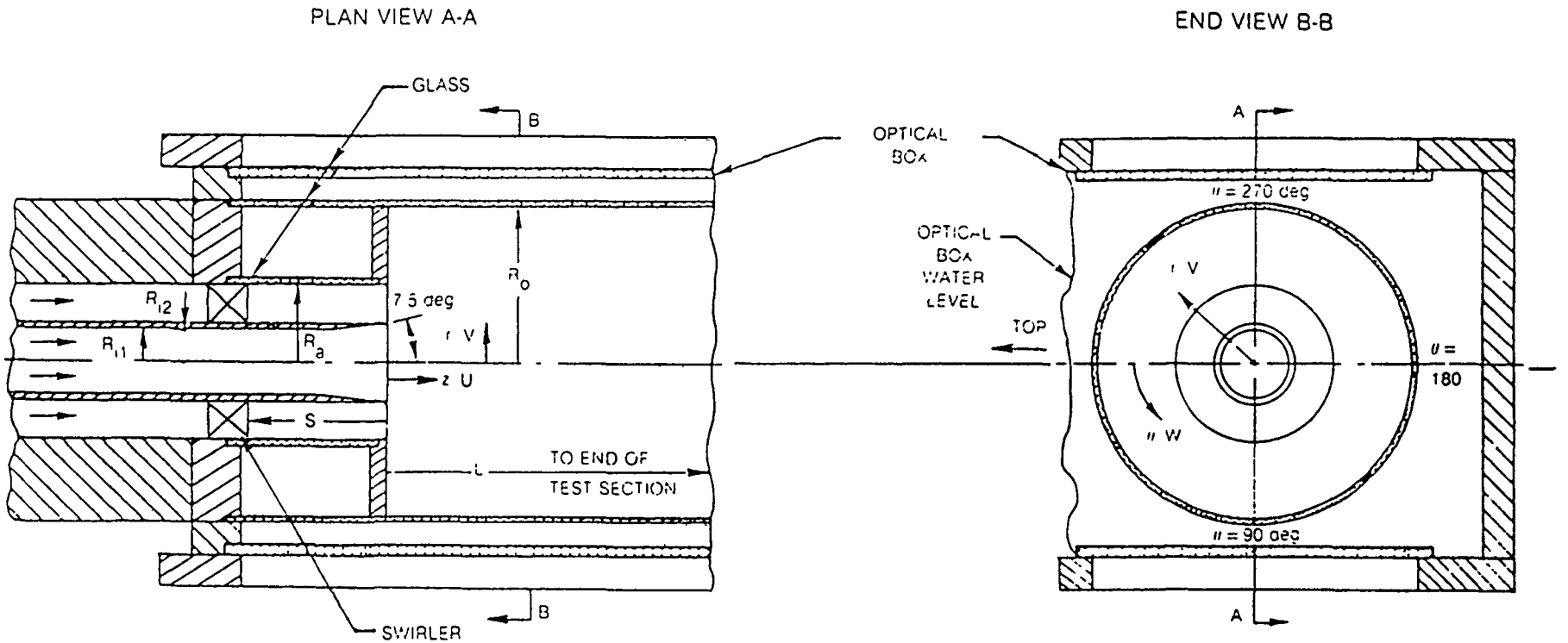

Figure 2. Sketch of Test Section Inlet Region (from Ref. 2).

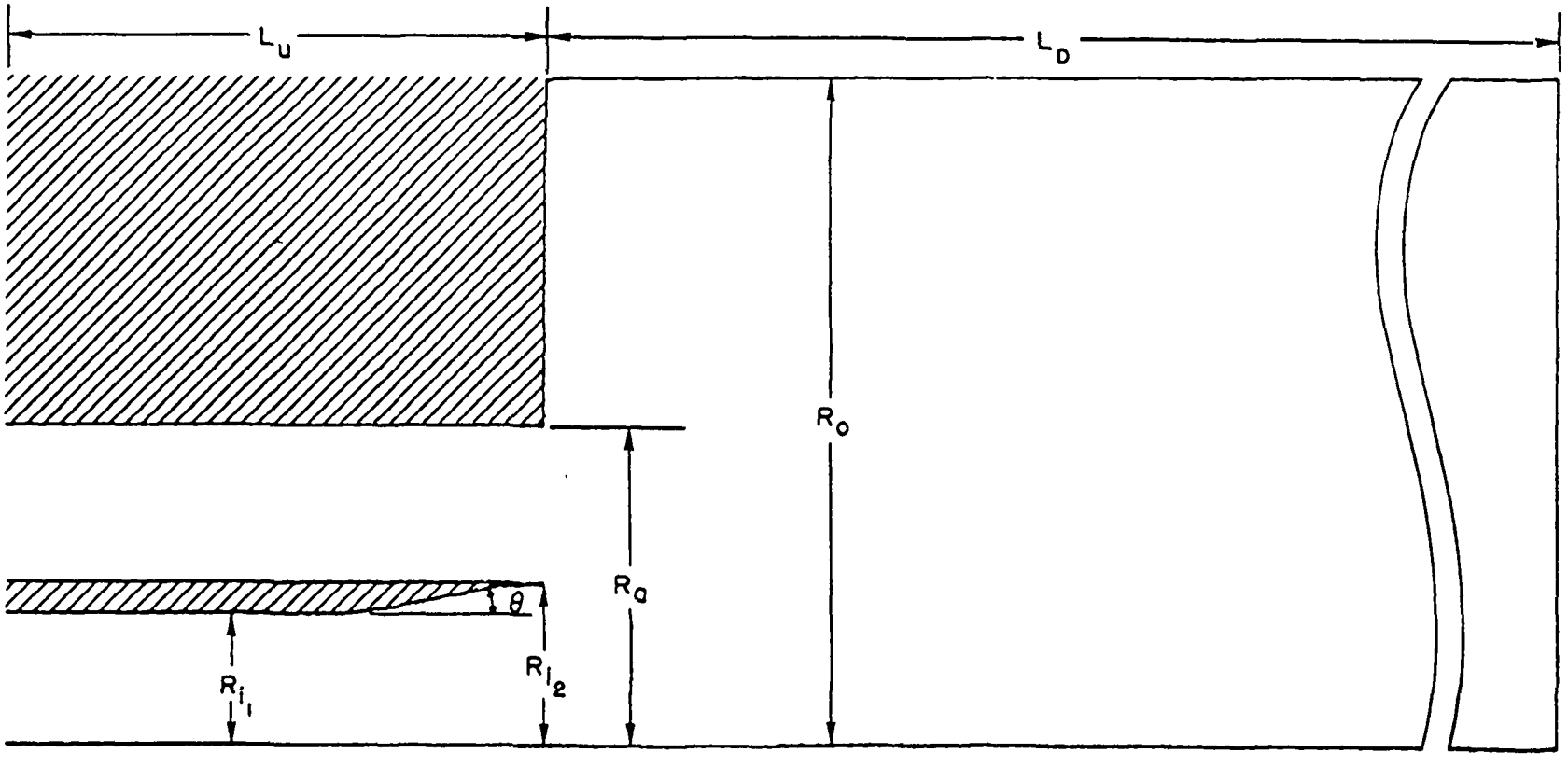

R_{i_1} = 12.5mm

R_{i_2} = 15.3mm

R_u = 29.5mm

R_o = 61.0mm

L_u = 51.0mm

L_D = 854.0mm

θ = 7.5°

Figure 3. Schematic of Computational Domain.

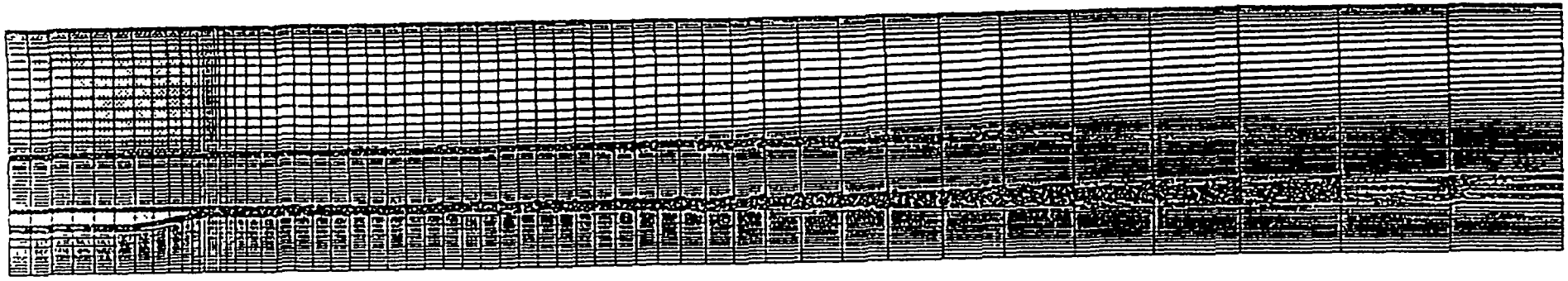

Figure 4. Computational Grid (Downstream Section not Shown).

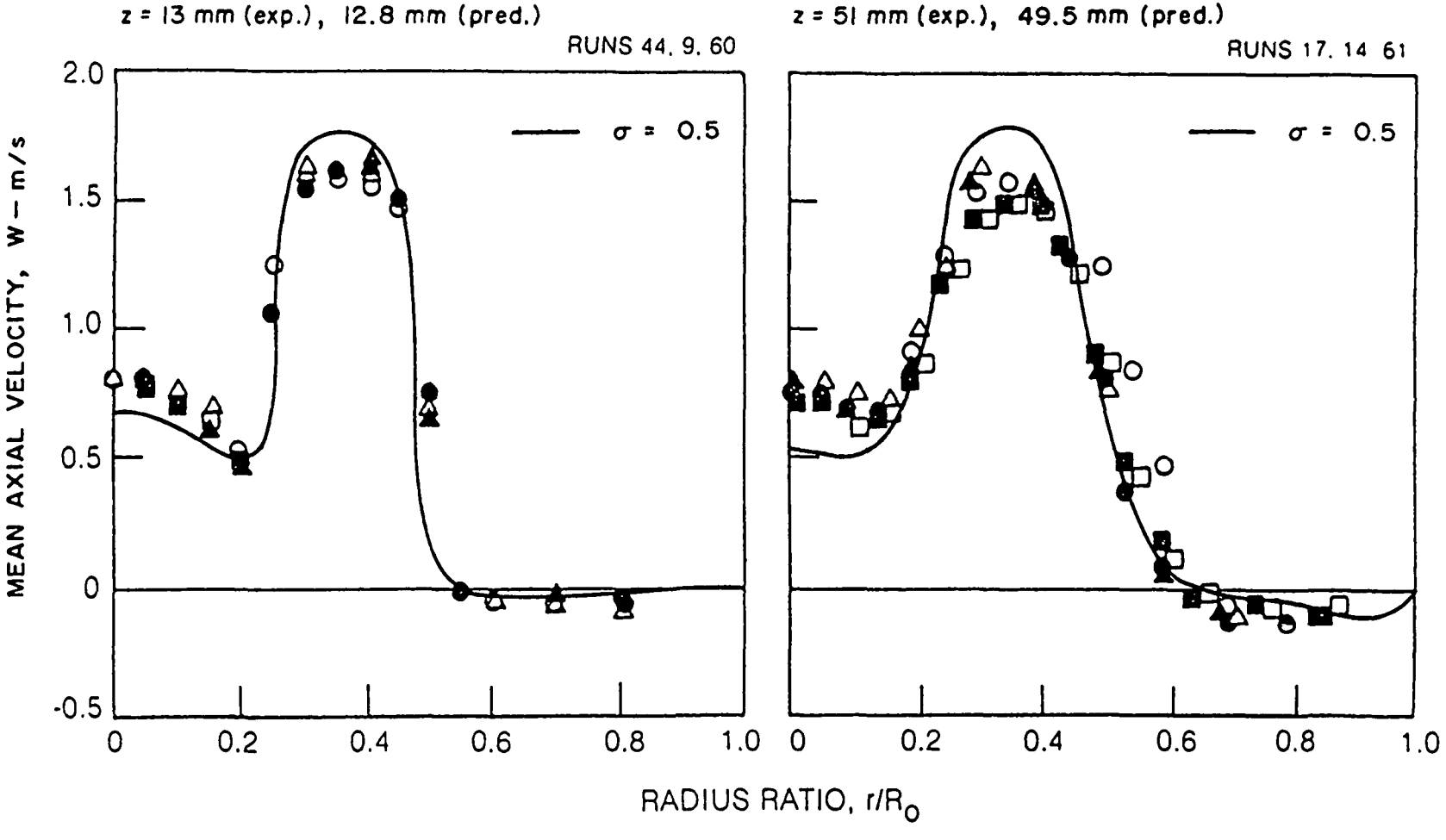

Figure 5. Axial Velocity Profiles for Nonswirling Flow.

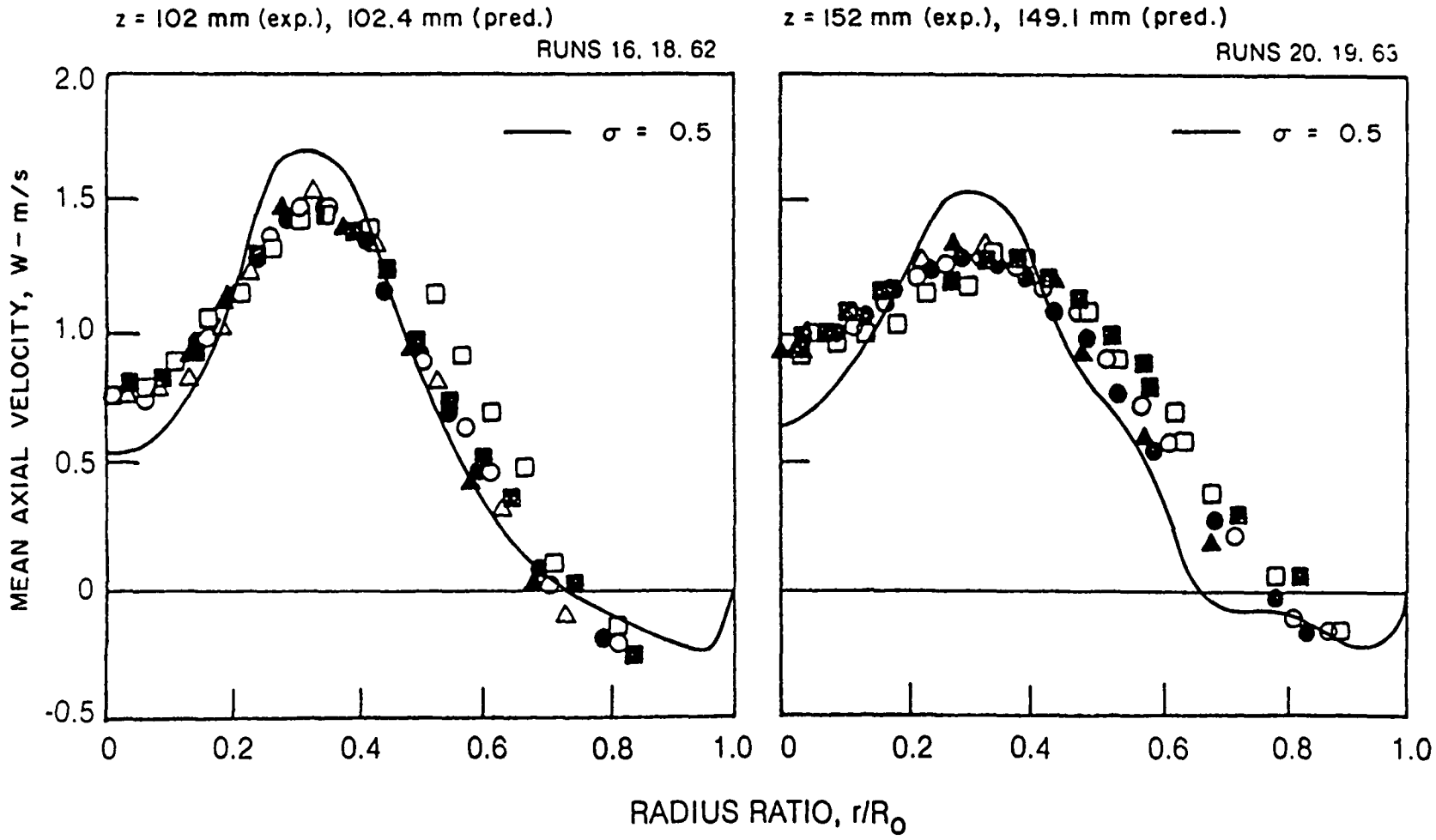

Figure 5(a). Axial Velocity Profiles for Nonswirling Flow.

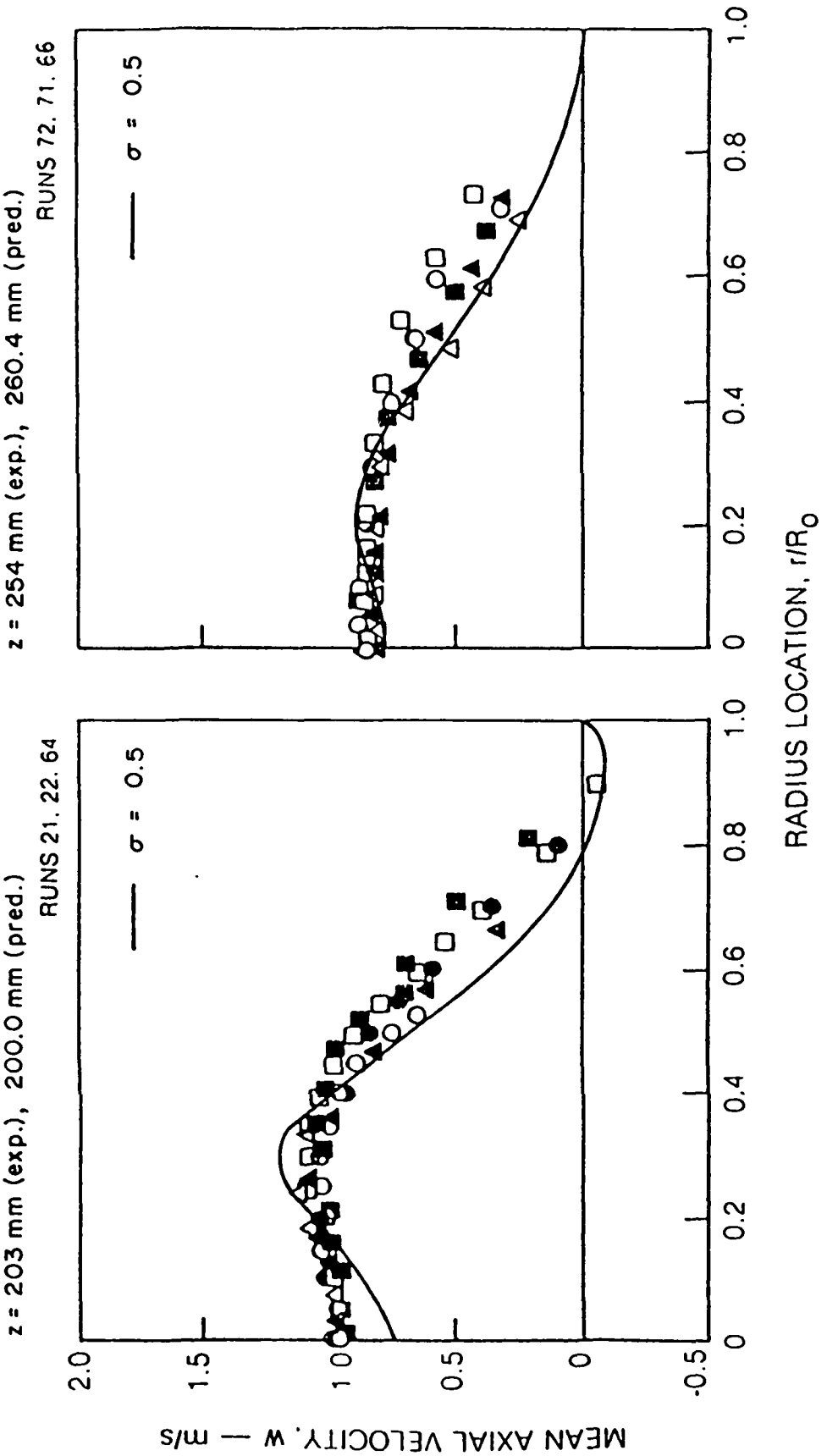

Figure 5(b). Axial Velocity Profiles for Nonswirling Flow.

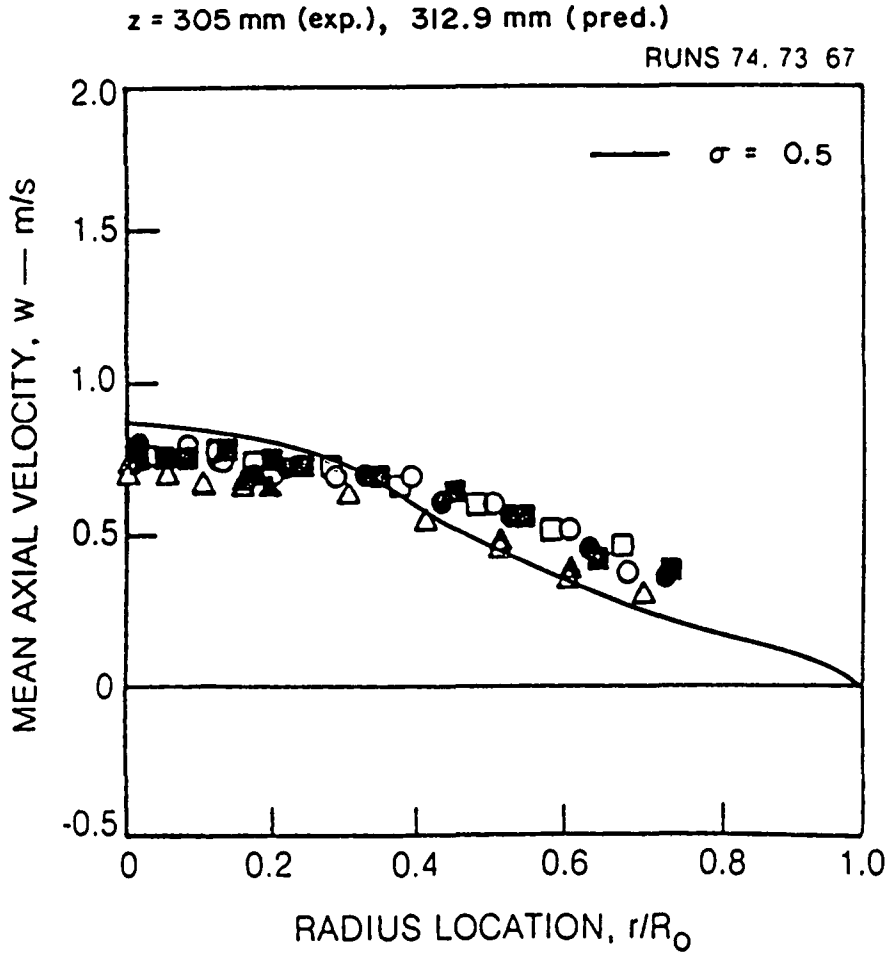

Figure 5(c). Axial Velocity Profiles for Nonswirling Flow.

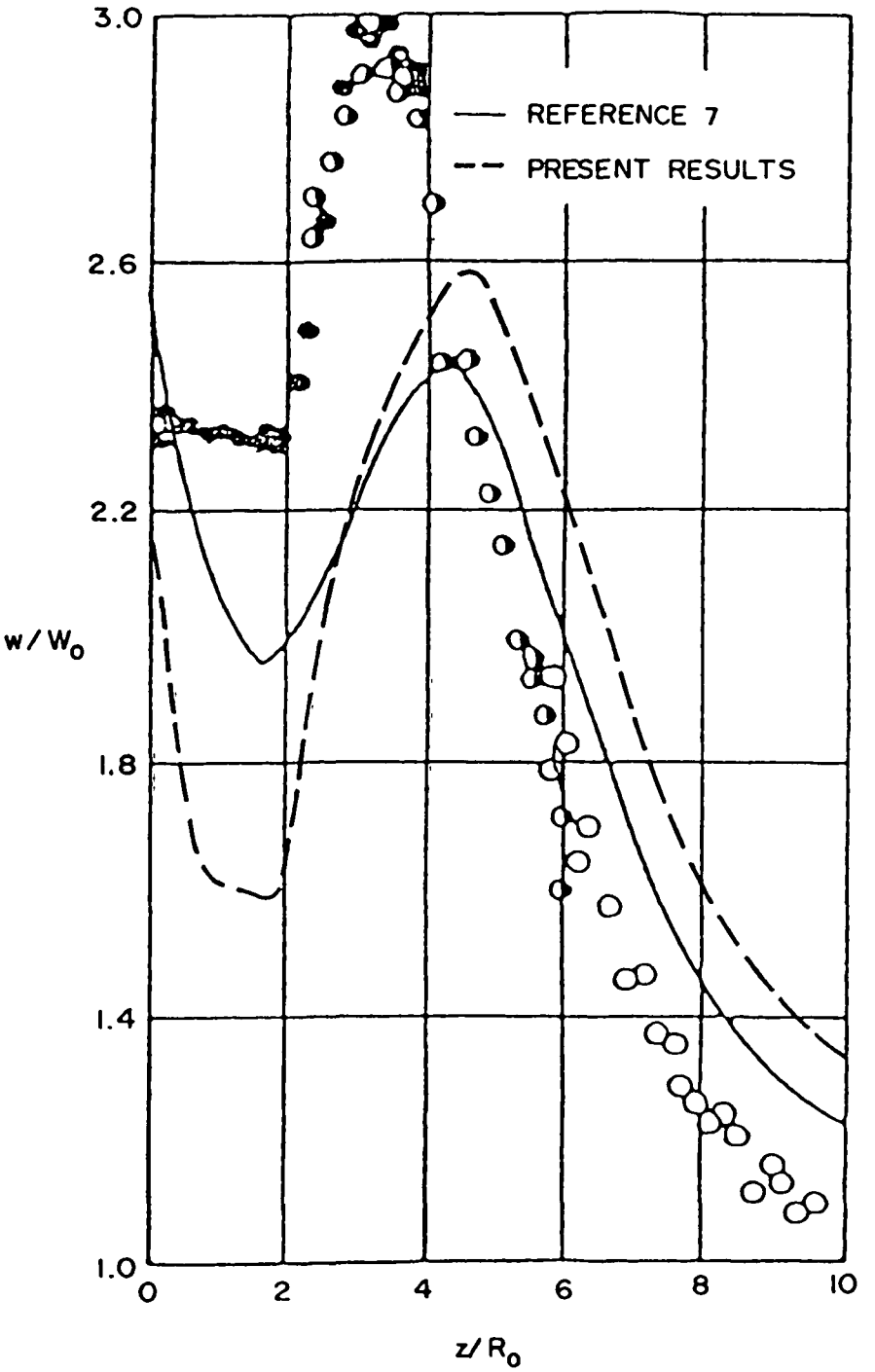

Figure 6. Mean Axial Velocity Distribution Along Duct Centerline Nonswirling Flow.

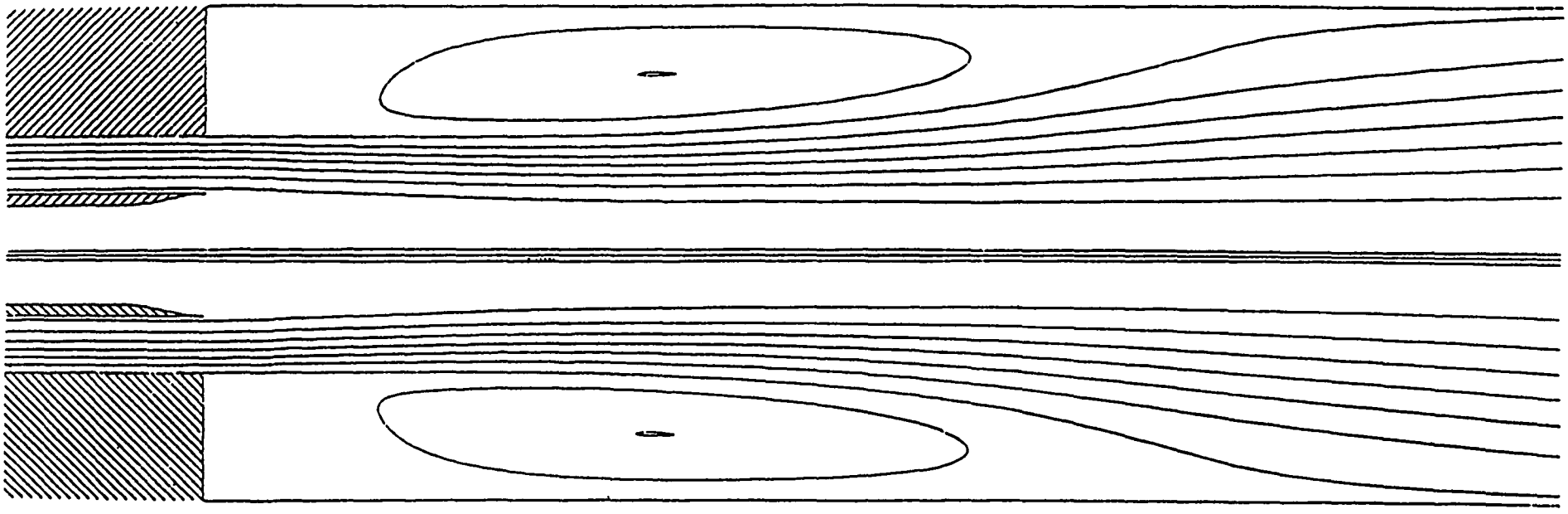

Figure 7. Streamline Pattern for Nonswirling Flow.

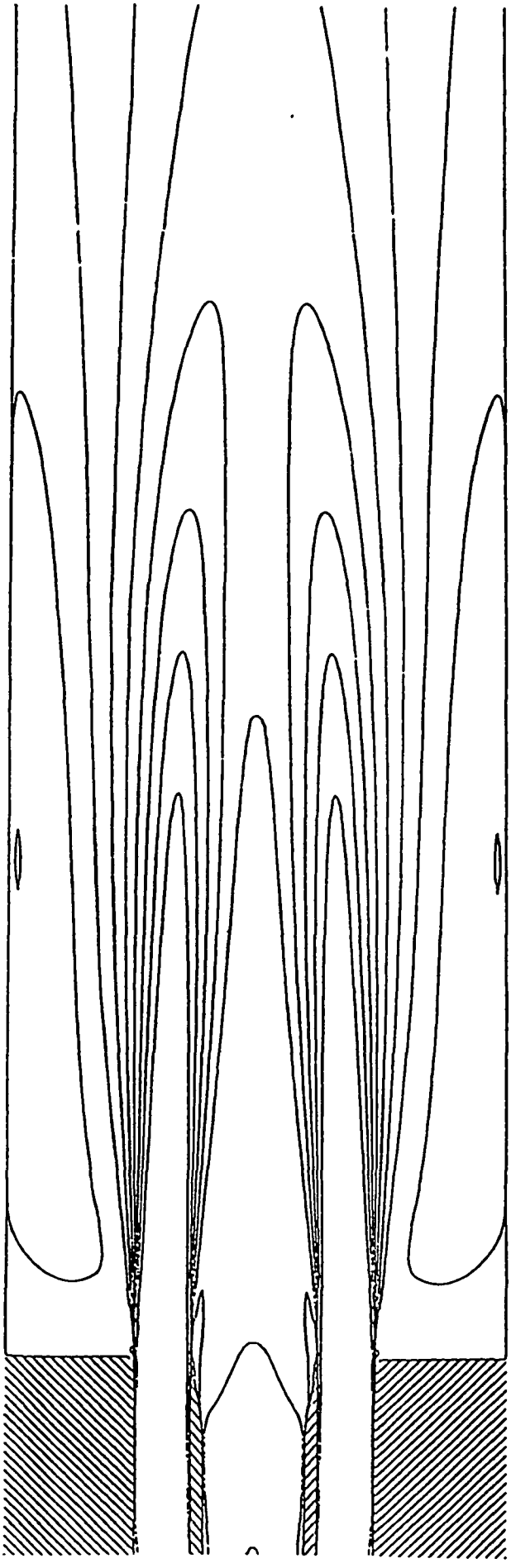

Figure 8. Contours of Constant Axial Velocity for Nonswirling Flow.

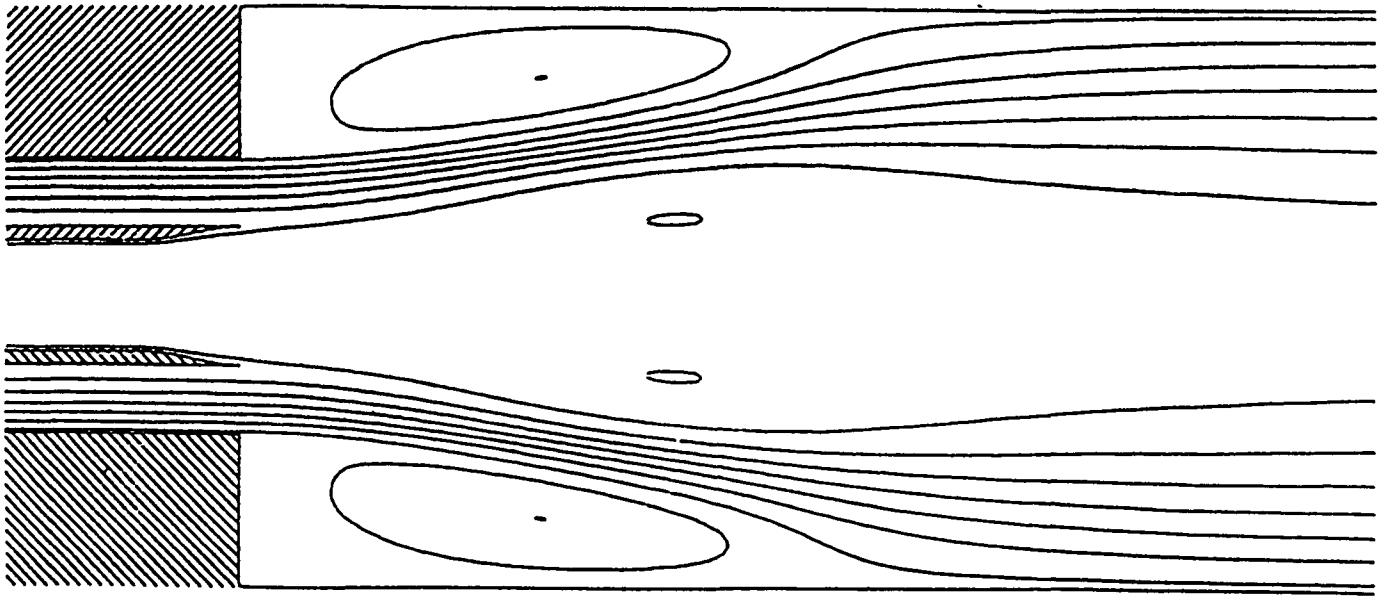

(b) $\sigma = .5$

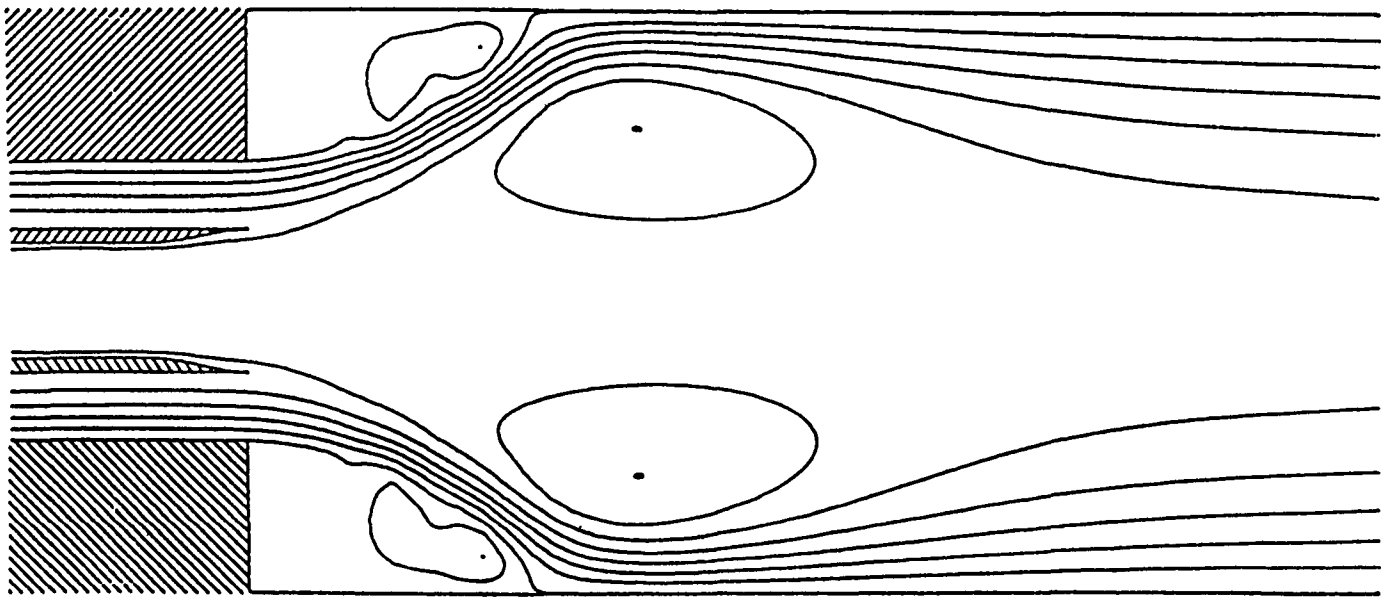

(a) $\sigma = .1$

Figure 9. Streamline Pattern for Swirling Flow.

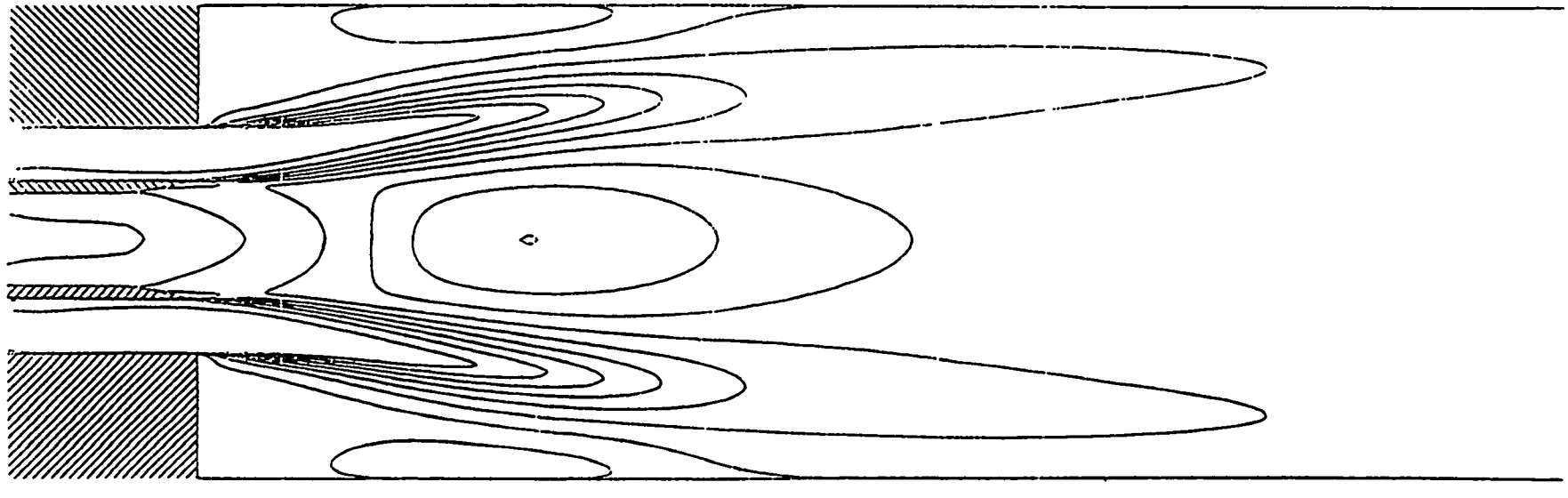

(b) $\sigma = .5$

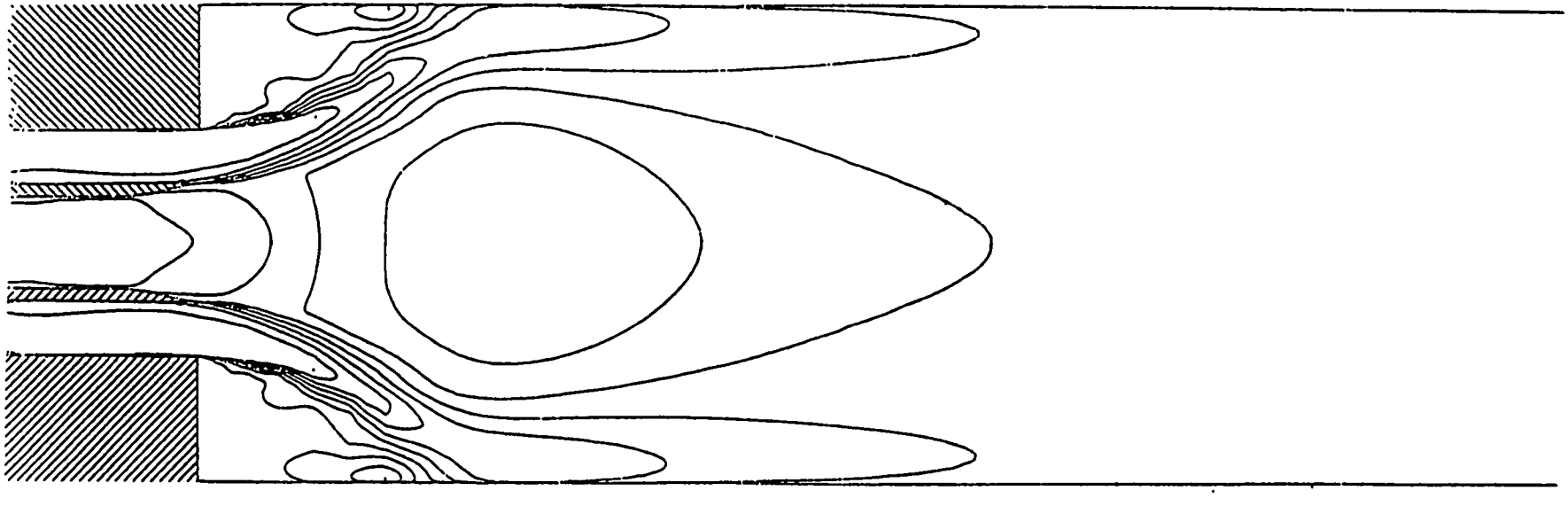

(a) $\sigma = .1$

Figure 10. Contours of Constant Axial Velocity for Swirling Flow.

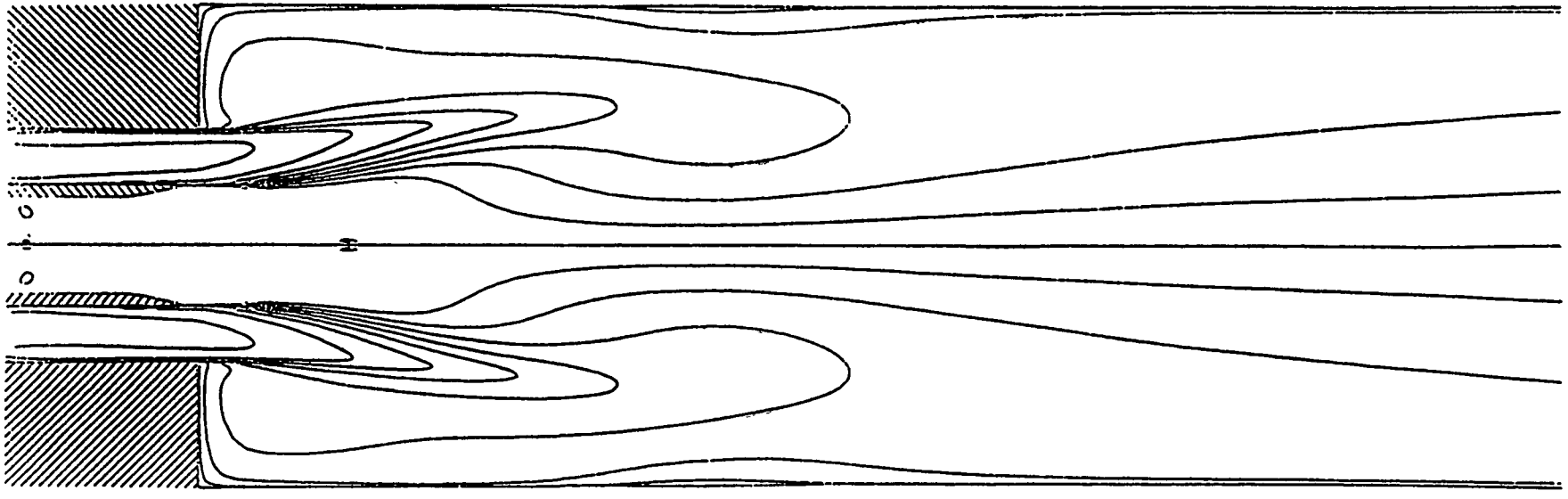

(b) $\sigma = .5$

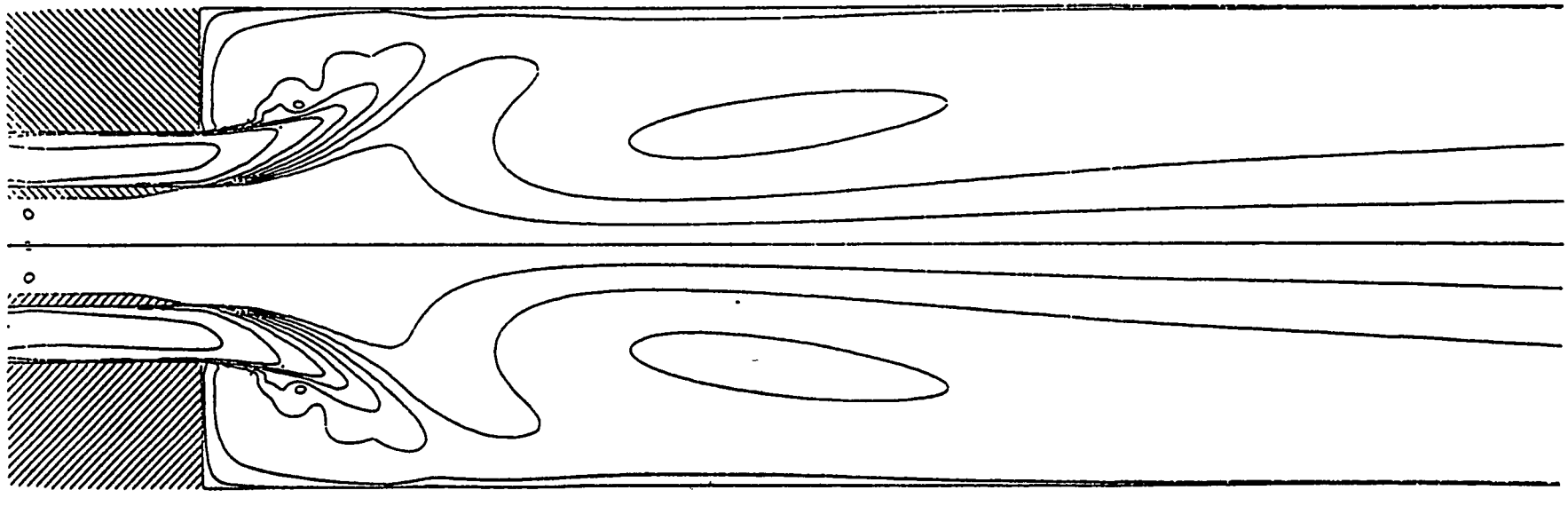

(a) $\sigma = .1$

Figure 11. Contours of Constant Azimuthal Velocity for Swirling Flow.

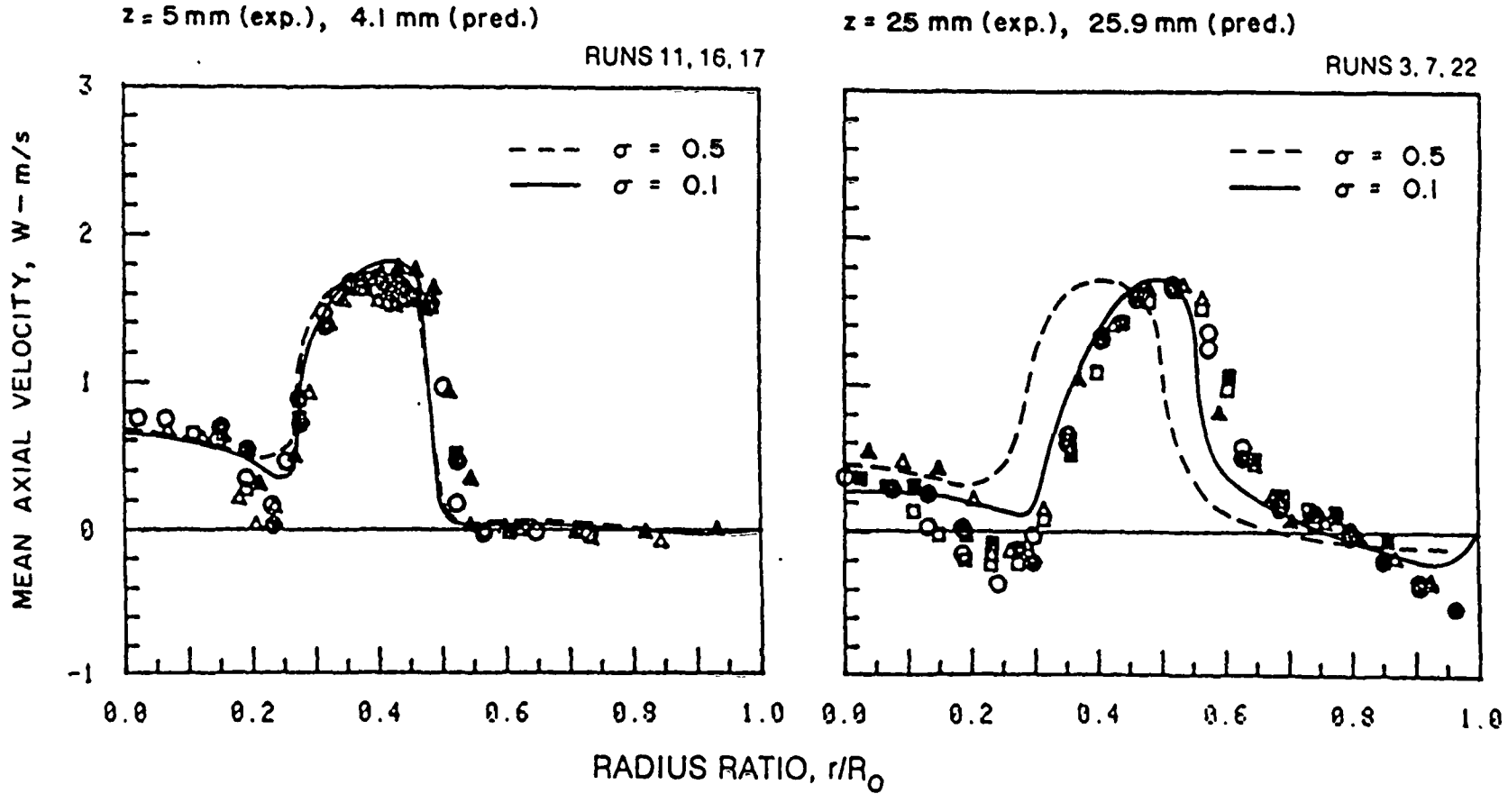

Figure 12. Mean Axial Velocity Profiles for Swirling Flow.

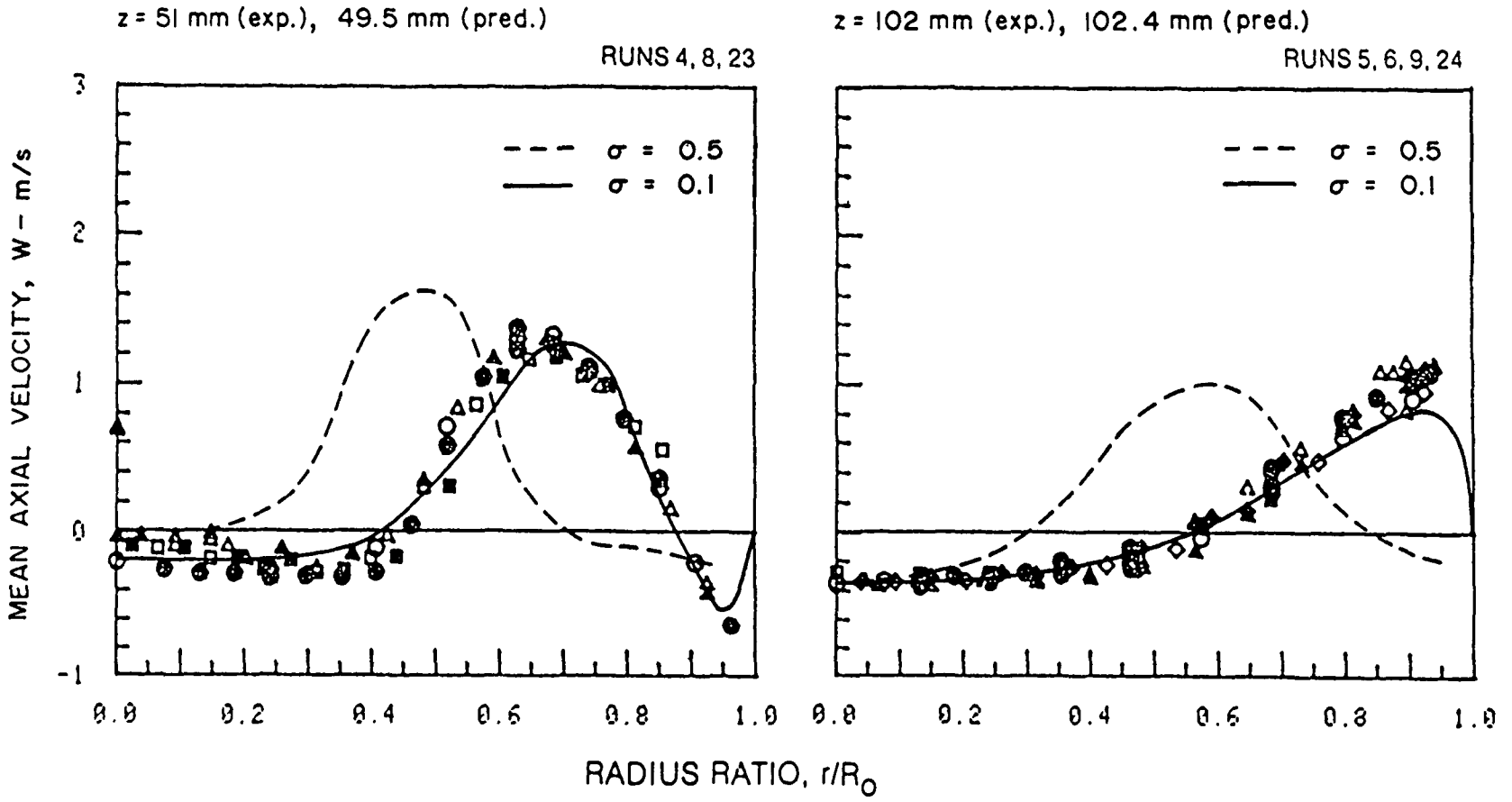

Figure 12(a). Mean Axial Velocity Profiles for Swirling Flow.

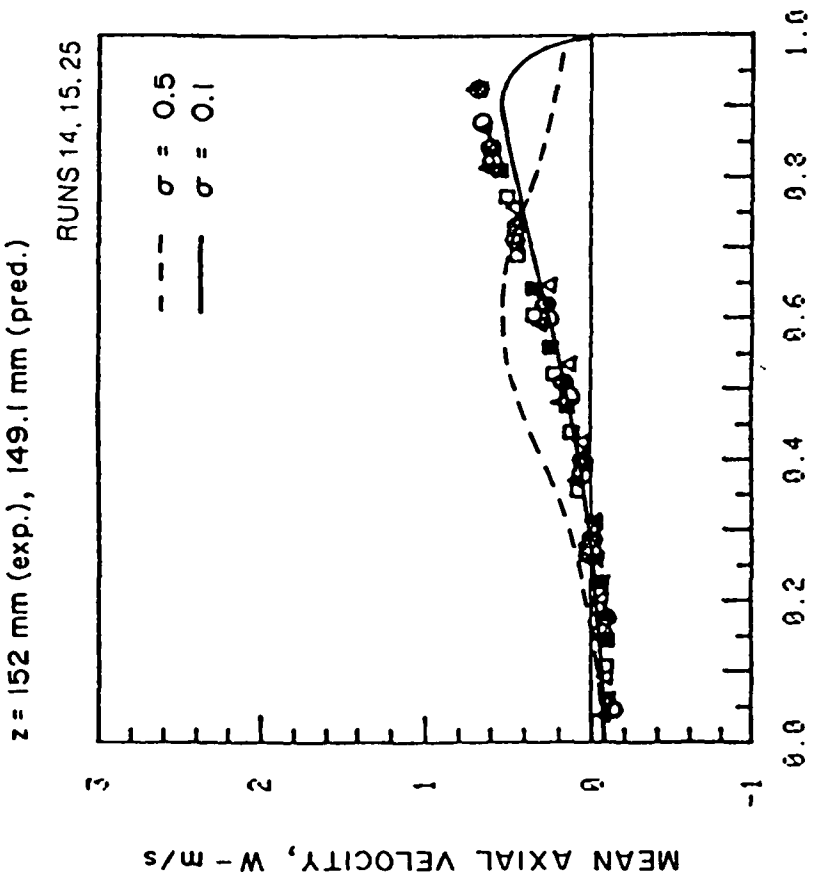

Figure 12(b). Mean Axial Velocity Profiles for Swirling Flow.

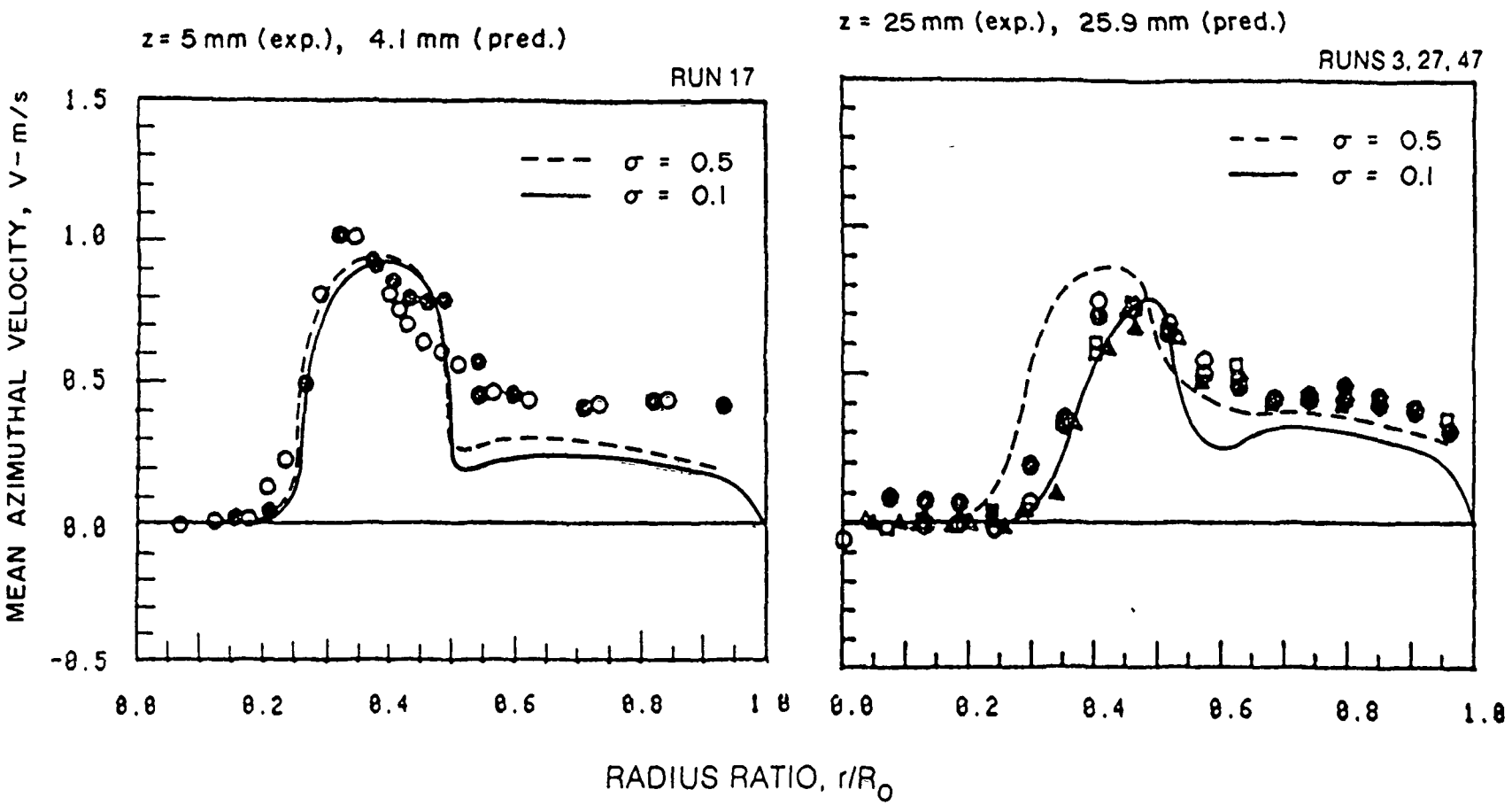

Figure 13. Mean Azimuthal Velocity Profiles for Swirling Flow.

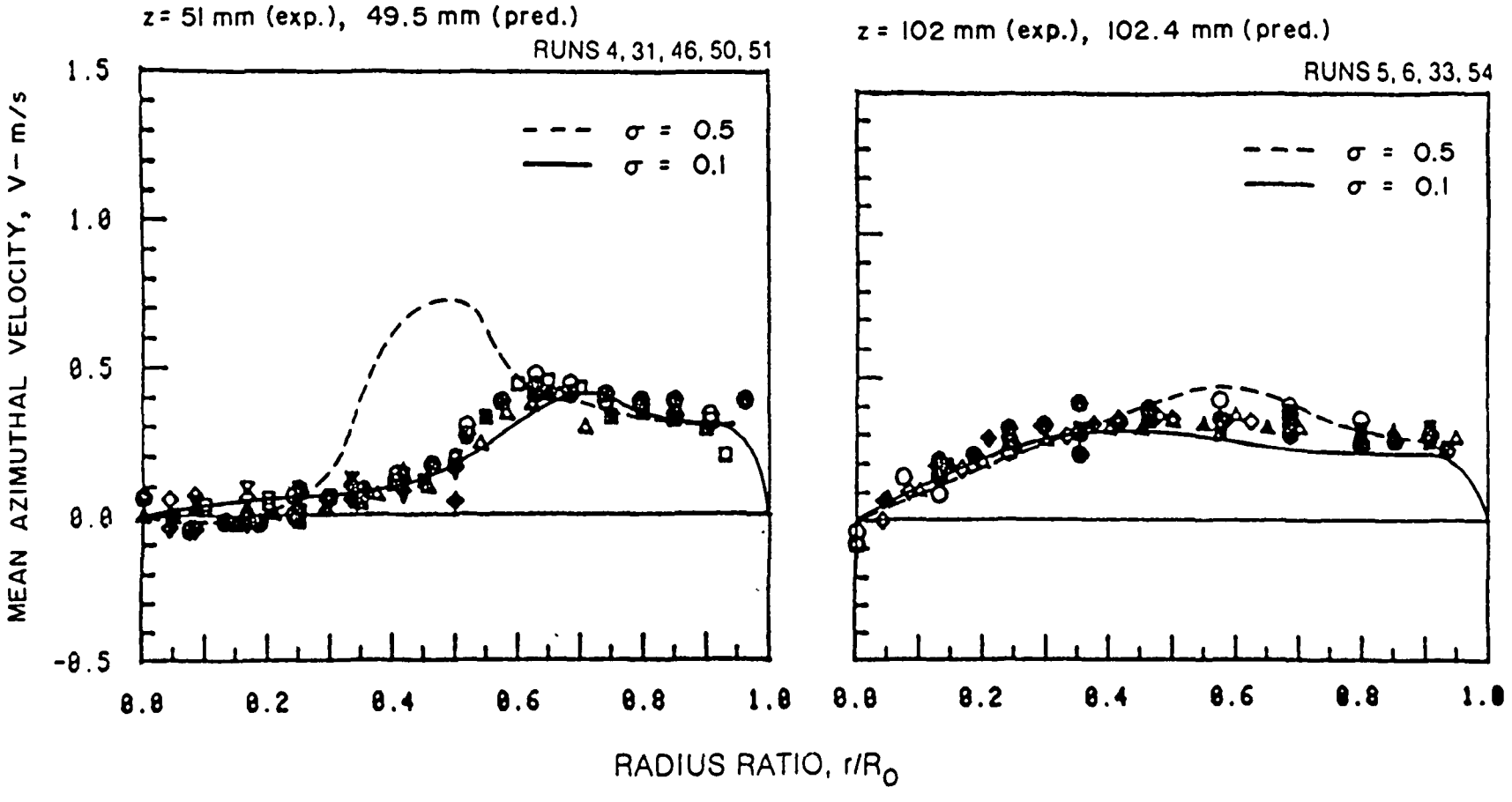

Figure 13(a). Mean Azimuthal Velocity Profiles for Swirling Flow.

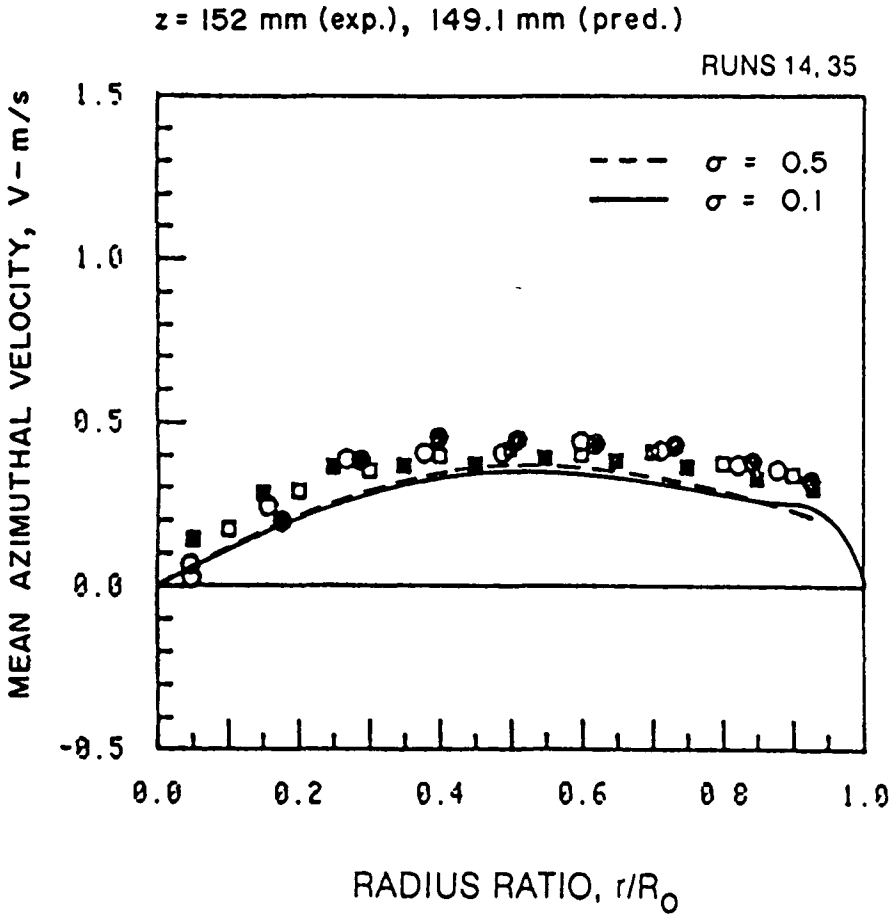

Figure 13(b). Mean Azimuthal Velocity Profiles for Swirling Flow.

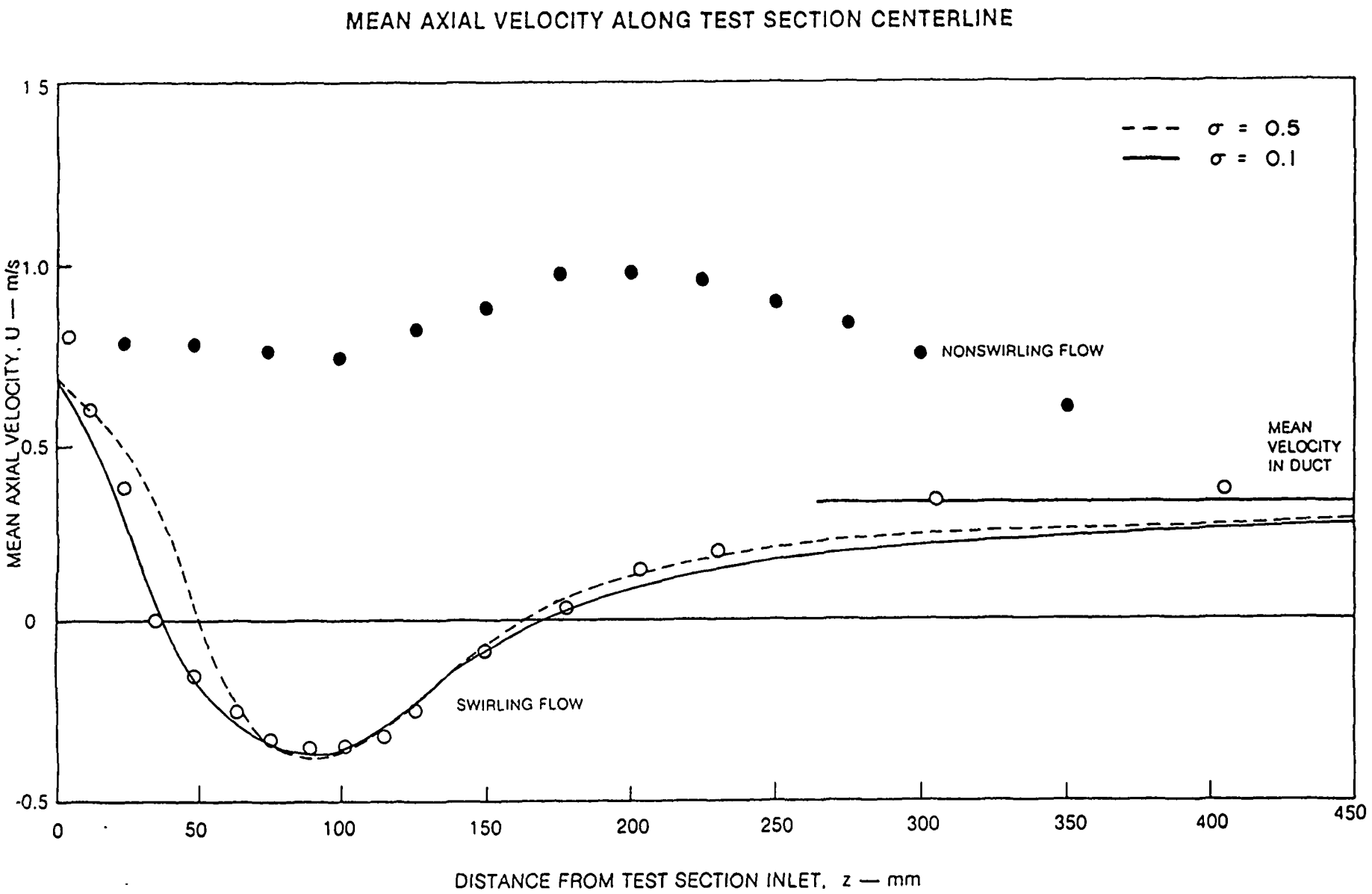

Figure 14. Mean Axial Velocity Along Test Section Centerline for Swirling Flow.

REFERENCES

1. Johnson, B.V. and Bennett, J.C.: Mass and Momentum Turbulent Transport Experiments with Confined Coaxial Jets, NASA CR-165574, 1981.

2. Roback, R. and Johnson, B.V.: Mass and Momentum Turbulent Transport Experiments with Confined Swirling Coaxial Jets, NASA CR-168252, 1983.

3. Johnson, B.V., Bennett, J.C., Syed, S.A. and Sturgess, G.: Velocity and Concentration Characteristics and their Cross Correlations for Coaxial Jets in a Confined Sudden Expansion, Parts I and II, presented at ASME Symposium on the Fluid Mechanics of Combustion Systems, June 1981.

4. Brondum, D. and Bennett, J.: The Influence of Large-Scale Motion on Turbulent Transport for Confined Coaxial Jets, Final Contracts' Report, NASA Grant NAG 3-350, March 1985.

5. Briley, W.R. and McDonald, H.: Solution of the Multi-Dimensional Compressible Navier-Stokes Equations by a Generalized Implicit Method, Journal of Computational Physics, Vol. 24, 1977.

6. Briley, W.R. and McDonald, H.: On the Structure and Use of Linearized Block Implicit Schemes, Journal of Computational Physics, Vol. 34, 1980.

7. Johnson, B.V. and Roback, R.: Mass and Momentum Turbulent Transport Experiments, presented at NASA HOST Meeting, October 1984.

8. Oh, Y.H.: An Analytical Transformation Technique for Generating Uniformly Spaced Computational Mesh in Numerical Grid Generation Techniques, NASA CP-2166, 1980.

9. Thomas, P.D. and Lombard, C.K.: Geometric Conservation Law and Its Application to Flow Computation on Moving Grids, AIAA Journal, Vol. 17, No. 10, 1979.

10. Kreskovsky, J.P., Shamroth, S.J. and McDonald, H.: Application of a General Boundary Layer Analysis to Turbulent Boundary Layers Subjected to Strong Favorable Pressure Gradients. J. Fluid Eng., Vol. 97, June 1975, pp. 217-224.

11. McDonald, H. and Fish, R.W.: Practical Calculation of Transitional Boundary Layers, Int. J. Heat and Mass Transfer, Vol. 16, No. 9, 1973.

12. Jones, W.P. and Launder, B.E.: The Prediction of Laminarization with a Two-Equation Model of Turbulence, Int. J. Heat and Mass Transfer, Vol. 15, 1972.

13. Shamroth, S.J. and Gibeling, H.J.: A Compressible Solution of the Navier-Stokes Equations for Turbulent Flow About an Airfoil, NASA CR-3183, 1979.

14. Launder, B.E. and Spalding, D.B.: The Numerical Computation of Turbulent Flows - Computer Methods in Applied Mechanics and Engineering,

15. Patel, V.C., Rodi, W. and Scheurer, G.: Evaluation of Turbulence Models for Near Wall and Low Reynolds Number Flows, Third Symposium on Turbulent Shear Flow, University of California, Davis, 1981.

16. Lindemuth, I. and Killeen, J.: Alternating Direction Implicit Techniques for Two-Dimensional Magnetohydrodynamic Calculations, Journal of Computational Physics, Vol. 13, 1973.

17. Douglas, J. and Gunn, J.E.: A General Formulation of Alternating Direction Methods, Numerische Math, Vol. 6, 1964, pp. 428-453.

18. Briley, W.R., Buggeln, R.C. and McDonald, H.: Computation of Laminar and Turbulent Flow in 90 Degree Square Duct and Pipe Bends Using the Navier-Stokes Equations, SRA Report R82-920009-F, 1982.

19. Shamroth, S.J. and McDonald, H.: An Assessment of an Ensemble-Averaged Navier-Stokes Calculation Procedure for Cascade Flow Fields, Scientific Research Associates Report R82-920011-F, 1982.

20. Shamroth, S.J., McDonald, H. and Briley, W.R.: A Navier-Stokes Solution for Transonic Flow Through a Cascade, SRA Report R81-920007-F, 1982.

21. Liu, N-S., Shamroth, S.J. and McDonald, H.: Numerical Solution of the Navier-Stokes Equations for Compressible Turbulent Two/Three-Dimensional Flows in the Terminal Shock Region of an Inlet/Diffuser, AIAA Paper 83-1892, 1983.

22. Bird, R.B., Stewart, W.E. and Lightfoot, E.N.: Transport Phenomena, John Wiley & Sons, 1960.

23. Beam, R.M. and Warming, R.F.: An Implicit Factored Scheme for Compressible Navier-Stokes Equations, AIAA Journal, Vol. 16, 1978.

24. Beam, R.M. and Warming, R.F.: An Implicit Finite Difference Algorithm for Hyperbolic Systems in Conservation Law Form, Journal of Computational Physics, Vol. 22, 1976.

25. Beam, R.M. and Warming, R.F.: Alternating Direction Implicit Methods for Parabolic Equations with a Mixed Derivative, SIAM J. Sci. Stat. Comp., Vol. 1, 1980.

APPENDIX A

The governing conservation equations in cylindrical-polar coordinates are transformed using the Jacobian transformation,

$$y^j = y^j(\bar{x}_1, \bar{x}_2, \bar{x}_3, t)$$
$$\tau = t \tag{A-1}$$

where $(\bar{x}_1, \bar{x}_2, \bar{x}_3) = (r, \theta, z)$. The resulting equations may be written in the following compact form:

$$\frac{\partial(J\vec{W})}{\partial\tau} = -\sum_{j=1}^{3} \frac{\partial}{\partial y^j}(J y^j_{,t}\vec{W}) - \sum_{i=1}^{3}\left\{\beta_i \frac{\partial}{\partial y^j}(J y^j_{,i}\vec{F}_i)\right.$$
$$\left. + \gamma_i \frac{\partial}{\partial y^j}(J y^j_{,i}\vec{P}_i) + \zeta_i \frac{\partial}{\partial y^j}(J y^j_{,i}\vec{G}_i)\right\} + J\vec{S} + J\vec{C} \tag{A-2}$$

where

$$y^j_{,t} \equiv \frac{\partial y^j}{\partial t}$$
$$y^j_{,i} \equiv \frac{\partial y^j}{\partial \bar{x}_i} \tag{A-3}$$

Further, the coefficients β_i, γ_i, ζ_i are given by

$$\beta_1 = \frac{1}{r}, \quad \beta_2 = \frac{1}{r}, \quad \beta_3 = 1$$
$$\gamma_1 = 1, \quad \gamma_2 = \frac{1}{r}, \quad \gamma_3 = 1 \tag{A-4}$$
$$\zeta_1 = \frac{1}{r^m}, \quad \zeta_2 = \frac{1}{r}, \quad \zeta_3 = 1$$

and m = 1 for all equations except the $\bar{x}_2$-direction momentum equations for which m = 2.

The vector variables used in Eq. (A-2) are defined as

$$\vec{W} = \begin{bmatrix} \rho U_1 \\ \rho U_2 \\ \rho U_3 \\ \rho \\ \rho h \\ \rho k \\ \rho \epsilon \end{bmatrix} \qquad \vec{F}_i = r^n \begin{bmatrix} \rho U_1 U_i \\ \rho U_2 U_i \\ \rho U_3 U_i \\ \rho U_i \\ \rho h U_i \\ \rho k U_i \\ \rho \epsilon U_i \end{bmatrix}$$

(A-5) (A-6)

where n = 1 for i = 1 and n = 0 for i = 2, 3.

$$\vec{G}_1 = \begin{bmatrix} r\tau_{11} \\ r^2\tau_{12} \\ r\tau_{13} \\ 0 \\ -rq_1 \\ \frac{\mu_T}{\sigma_k}\gamma_1 k_{,1} \\ \frac{\mu_T}{\sigma_k}\gamma_1 \epsilon_{,1} \end{bmatrix} \qquad \vec{P}_i = \begin{bmatrix} p\delta_{i1} \\ p\delta_{i2} \\ p\delta_{i3} \\ 0 \\ 0 \\ 0 \\ 0 \end{bmatrix} \qquad \vec{G}_i = \begin{bmatrix} \tau_{i1} \\ \tau_{i2} \\ \tau_{i3} \\ 0 \\ -q_i \\ \frac{\mu_T}{\sigma_k}\gamma_i k_{,i} \\ \frac{\mu_T}{\sigma_k}\gamma_i \epsilon_{,i} \end{bmatrix} \quad \text{for } i = 2,3$$

(A-7) (A-8) (A-9)

Note that the velocity componetns (U_1, U_2, U_3) are the cylindrical-polar velocity components written in cylindrical-polar coordinates. The molecular and turbulent stress tensors may be written as

$$\tau_{ij} = 2\mu_{eff}\bar{D}_{ij} - \frac{2}{3}\mu_{eff}(\nabla\cdot\vec{U})\delta_{ij} + \frac{2}{3}(K_B\nabla\cdot\vec{U} - \rho k)\delta_{ij} \qquad \text{(A-10)}$$

and the rate of strain tensor components in cylindrical-polar coordinates are

$$\bar{D}_{11} = \frac{\partial U_1}{\partial \bar{x}_1}$$

$$\bar{D}_{22} = \frac{1}{r}\frac{\partial U_2}{\partial \bar{x}_2} + \frac{U_1}{r}$$

$$\bar{D}_{33} = \frac{\partial U_3}{\partial \bar{x}_3}$$

$$\bar{D}_{12} = \frac{1}{2}\left[r\frac{\partial}{\partial \bar{x}_1}\left(\frac{U_2}{r}\right) + \frac{1}{r}\frac{\partial U_1}{\partial \bar{x}_2} \right] \qquad \text{(A-11)}$$

$$\bar{D}_{13} = \frac{1}{2}\left[\frac{\partial U_3}{\partial \bar{x}_1} + \frac{\partial U_1}{\partial \bar{x}_3} \right]$$

$$\bar{D}_{23} = \frac{1}{2}\left[\frac{1}{r}\frac{\partial U_3}{\partial \bar{x}_2} + \frac{\partial U_2}{\partial \bar{x}_3} \right]$$

and

$$\nabla \cdot \vec{U} = \frac{1}{r}\frac{\partial}{\partial \bar{x}_1}(rU_1) + \frac{1}{r}\frac{\partial U_2}{\partial \bar{x}_2} + \frac{\partial U_3}{\partial \bar{x}_3} \qquad \text{(A-12)}$$

The derivatives required in Eqs. (A-11) and (A-12) must be expressed in terms of the computational coordinates y^j using the chain rule.

Finally, the vecotr $\vec{S}$ contains source terms and certain differential terms which do not conform to the basic structure of Eq. (A-2), and the vector $\vec{C}$ contains the additional curvature terms due to the cylindrical-polar coordinate system.

$$\vec{S} = \begin{bmatrix} 0 \\ 0 \\ 0 \\ 0 \\ \dfrac{D(\rho)}{Dt} + \Phi + \rho\epsilon \\ \mu_T\left[2\bar{D}_{ij}\bar{D}_{ij}\right] - \rho\epsilon - 2\rho\nu(\nabla k^{1/2})^2 \\ C_1\dfrac{\epsilon}{k}\left[\mu_T(2\bar{D}_{ij}\bar{D}_{ij}) + 2\mu\mu_T(\nabla^2 U)^2 - C_2\rho\dfrac{\epsilon^2}{k}\right] \end{bmatrix} \qquad \text{(A-13)}$$

$$\vec{C} = \begin{bmatrix} \frac{1}{r} \rho U_2^2 - \frac{1}{r} \bar{\tau}_{22} \\ -\frac{1}{r} \rho U_1 U_2 \\ 0 \\ 0 \\ 0 \\ 0 \\ 0 \end{bmatrix} \qquad \text{(A-14)}$$

APPENDIX B - SOLUTION PROCEDURE

Background

The solution procedure employs a consistently-split linearized block implicit (LBI) algorithm which has been discussed in detail in [5, 6]. There are two important elements of this method:

(1) the use of a noniterative formal time linearization to produce a fully-coupled linear multidimensional scheme which is written in "block implicit" form; and

(2) solution of this linearized coupled scheme using a consistent "splitting" (ADI scheme) patterned after the Douglas-Gunn [17] treatment of scalar ADI schemes.

The method is thus referred to as a split linearized block implicit (LBI) scheme. The method has several attributes:

(1) the noniterative linearization is efficient;

(2) the fully-coupled linearized algorithm eliminates instabilities and/or extremely slow convergence rates often attributed to methods which employ ad hoc decoupling and linearization assumptions to identify nonlinear coefficients which are then treated by lag and update techniques;

(3) the splitting or ADI technique produces an efficient algorithm which is stable for large time steps and also provides a means for convergence acceleration for further efficiency in computing steady solutions;

(4) intermediate steps of the splitting are consistent with the governing equations, and this means that the "physical" boundary conditions can be used for the intermediate solutions. Other splittings which are inconsistent can have several difficulties in satisfying physical boundary conditions [6].

(5) the convergence rate and overall efficiency of the algorithm are much less sensitive to mesh refinement and redistribution than algorithms based on explicit schemes or which employ ad hoc decoupling and linearization assumptions. This is important for accuracy and for computing turbulent flows with viscous sublayer resolution; and

(6) the method is general and is specifically designed for the complex systems of equations which govern multiscale viscous flow in complicated geometries.

This same algorithm was later considered by Beam and Warming [23], but the ADI splitting was derived by approximate factorization instead of the Douglas-Gunn procedure. They refer to the algorithm as a "delta form" approximate factorization scheme. This scheme replaced an earlier non-delta form scheme [24], which has inconsistent intermediate steps.

Split LBI Algorithm

Linearization and Time Differencing

The system of governing equations to be solved consists of three/four equations: continuity and two/three components of momentum equation in three/four dependent variables: ρ, u, v, w. Using notation similar to that in [5], at a single grid point this system of equations can be written in the following form:

$$\partial H(\phi)/\partial t = D(\phi) + S(\phi) \qquad (1)$$

where ϕ is the column-vector of dependent variables, H and S are column-vector algebraic functions of ϕ, and D is a column vector whose elements are the spatial differential operators which generate all spatial derivatives appearing in the governing equation associated with that element.

The solution procedure is based on the following two-level implicit time-difference approximations of (1):

$$(H^{n+1} - H^n)/\Delta t = \beta(D^{n+1} + S^{n+1}) \quad (1-\beta)(D^n + S^n) \qquad (2)$$

where, for example, H^{n+1} denotes $H(\phi^{n+1})$ and $\Delta t = t^{n+1} - t^n$. The parameter β ($0.5 \leq \beta \leq 1$) permits a variable time-centering of the scheme, with a truncation error of order $[\Delta t^2, (\beta - 1/2)\,\Delta t]$.

A local time linearization (Taylor expansion about ϕ^n) of requisite formal accuracy is introduced, and this serves to define a linear differential operator L (cf. [5]) such that

$$D^{n+1} = D^n + L^n(\phi^{n+1} - \phi^n) + O(\Delta t^2) \qquad (3)$$

Similarly,

$$H^{n+1} = H^n + (\partial H/\partial \phi)^n (\phi^{n+1} - \phi^n) + O(\Delta t^2) \qquad (4)$$

$$S^{n+1} = S^n + (\partial S/\partial \phi)^n (\phi^{n+1} - \phi^n) + O(\Delta t^2) \qquad (5)$$

Eqs. (3-5) are inserted into Eq. (2) to obtain the following system which is linear in ϕ^{n+1}

$$(A - \beta\Delta t\ L^n)\ (\phi^{n+1} - \phi^n) = \Delta t\ (D^n + S^n) \qquad (6)$$

and which is termed a linearized block implilcit (LBI) scheme. Here, A denotes a matrix defined by

$$A \equiv (\partial H/\partial\phi)^n - \beta\Delta t\ (\partial S/\partial\phi)^n \qquad (7)$$

Eq. (6) has 0 (Δt) accuracy unless $H \equiv \phi$, in which case the accuracy is the same as Eq. (2).

Special Treatment of Diffusive Terms

The time differencing of diffusive terms is modified to accomodate cross-derivative terms and also turbulent viscosity and artificial dissipation coefficients which depend on the solution variables. Although formal linearization of the convection and pressure gradient terms and the resulting implicit coupling of variables is critical to the stability and rapid convergence of the algorithm, this does not appear to be important for the turbulent viscosity and artificial dissipation coefficients. Since the relationship between μ_e and d_j and the mean flow variables is not conveniently linearized, these diffusive coefficients are evaluated explicitly at t^n during each time step. Notationally, this is equivalent to neglecting terms proportional to $\partial\ \mu_e/\partial\phi$ or $\partial d_j/\partial\phi$ in L^n, which are formally present in the Taylor expansion (2), but retaining all terms proportional to μ_e or d_j in both L^n and D^n.

It has been found through extensive experience that this has little if any effect on the performance of the algorithm. This treatment also has the added benefit that the turbulence model equations can be decoupled from the system of mean flow equations by an appropriate matrix partitioning (cf. [6]) and solved separately in each step of the ADI solution procedure. This reduces the block size of the block tridiagonal systems which must be solved in each step and thus reduces the computational labor.

In addition, the viscous terms in the present formulation include a number of spatial cross-derivative terms. Although it is possible to treat cross-derivative terms implicitly within the ADI treatment which follows, it is not at all convenient to do so; and consequently, all cross-derivative terms are evaluated explicitly at t^n. For a scalar model equation representing combined convection and diffusion, it has been shown by Beam and

Warming [25] that the explicit treatment of cross-derivative terms does not degrade the unconditional stability of the present algorithm. To preserve notational simplicity, it is understood that all cross-derivative terms appearing in L^n are neglected but are retained in D^n. It is important to note that neglecting terms in L^n has no effect on steady solutions of Eq. (7), since $\phi^{n+1} - \phi^n \equiv 0$, and thus Eq. (7) reduces to the steady form of the equations: $D^n + S^n = 0$. Aside from stability considerations, the only effort of neglecting terms in L^n is to introduce an $0(\Delta t)$ truncation error.

Consistent Splitting of the LBI Scheme

To obtain an efficient algorithm, the linearized system (7) is split using ADI techniques. To obtain the split scheme, the multidimensional operator L is rewritten as the sum of three "one-dimensional" sub-operators L_i ($i = 1, 2, 3$) each of which contains all terms having derivatives with respect to the i-th coordinate. The split form of Eq. (7) can be derived either as in [5, 6] or by following the procedure described by Douglas and Gunn [17] in their generalization and unification of scalar ADI schemes, or using approximate factorization. For the present system of equations, the split algorithm is given by

$$(A - \beta\Delta t L_1^n)(\phi^* - \phi^n) = \Delta t\,(D^n + S^n) \qquad (8a)$$

$$(A - \beta\Delta t L_2^n)(\phi^{**} - \phi^n) = A\,(\phi^* - \phi^n) \qquad (8b)$$

$$(A - \beta\Delta t L_3^n)(\phi^{n+1} - \phi^n) = A\,(\phi^{**} - \phi^n) \qquad (8c)$$

where ϕ^* and ϕ^{**} are consistent intermediate solutions. If spatial derivatives appearing in L_i and D are replace by three-point difference formulas, as indicated previously, then each step in Eqs. (10a-c) can be solved by a block-tridiagonal elimination.

Combining Eqs. (8 a-c) gives

$$(A - \beta\Delta t L_1^n)\,A^{-1}\,(A - \beta\Delta t L_2^n)\,A^{-1}\,(A - \beta\Delta t L_3^n)(\phi^{n+1} - \phi^n) = \Delta t\,(D^n + S^n) \qquad (9)$$

which approximates the unsplit scheme (8) to $0(\Delta t^2)$. Since the intermediate steps are also consistent approximations for Eq. (8), physical boundary conditions can be used for ϕ^* and ϕ^{**} [5, 6]. Finally, since the L_i are homogeneous operators, it follows from Eqs. (8 a-c) that steady solutions have the property that $\phi^{n+1} = \phi^* = \phi^{**} = \phi^n$ and satisfy

$$D^n + S^n = 0 \qquad (10)$$

The steady solution thus depends only on the spatial difference approximations used for (10), and does not depend on the solution algorithm itself.

1 Report No	2 Government Accession No	3 Recipient's Catalog No
NASA CR-175036		

4 Title and Subtitle	5 Report Date
Influence of Large-Scale Motion on Turbulent Transport for Confined Coaxial Jets. Volume II - Navier-Stokes Calculations of Swirling and Nonswirling Confined Coaxial Jets	January 1986
	6 Performing Organization Code
7 Author(s)	8 Performing Organization Report No
Bernard C. Weinberg and Henry McDonald	None
	10 Work Unit No
9 Performing Organization Name and Address	11 Contract or Grant No
Scientific Research Associates P.O. Box 498 Glastonbury, Connecticut 06033	NAG 3-350
	13 Type of Report and Period Covered
12 Sponsoring Agency Name and Address	Contractor Report
National Aeronautics and Space Administration Washington, D.C. 20546	14 Sponsoring Agency Code
	505-31-42

15 Supplementary Notes

Final report. Project Manager, C. John Marek, Altitude Wind Tunnel Project Office, NASA Lewis Research Center, Cleveland, Ohio 44135.

16 Abstract

The existence of large-scale coherent structures in turbulent shear flows has been well documented. Discrepancies between experimental and computational data suggest a necessity to understand the roles they play in mass and momentum transport. Using conditional sampling and averaging on coincident two-component velocity and concentration-velocity experimental data for swirling and nonswirling coaxial jets, triggers for identifying the structures were examined. Concentration fluctuation was found to be an adequate trigger or indicator for the concentration-velocity data, but no suitable detector was located for the two-component velocity data. The large-scale structures are found in the region where the largest discrepancies exist between model and experiment. The traditional gradient transport model does not fit in this region as a result of these structures. The large-scale motion was found to be responsible for a large percentage of the axial mass transport. The large-scale structures were found to convect downstream at approximately the mean velocity of the overall flow in the axial direction. The radial mean velocity of the structures was found to be substantially greater than that of the overall flow.

17 Key Words (Suggested by Author(s))	18 Distribution Statement
Shear layers; Coaxial jets; Large-scale coherent structures	Unclassified - unlimited STAR Category 07

19 Security Classif (of this report)	20 Security Classif (of this page)	21 No of pages	22 Price*
Unclassified	Unclassified	56	A04

*For sale by the National Technical Information Service, Springfield, Virginia 22161

NASA